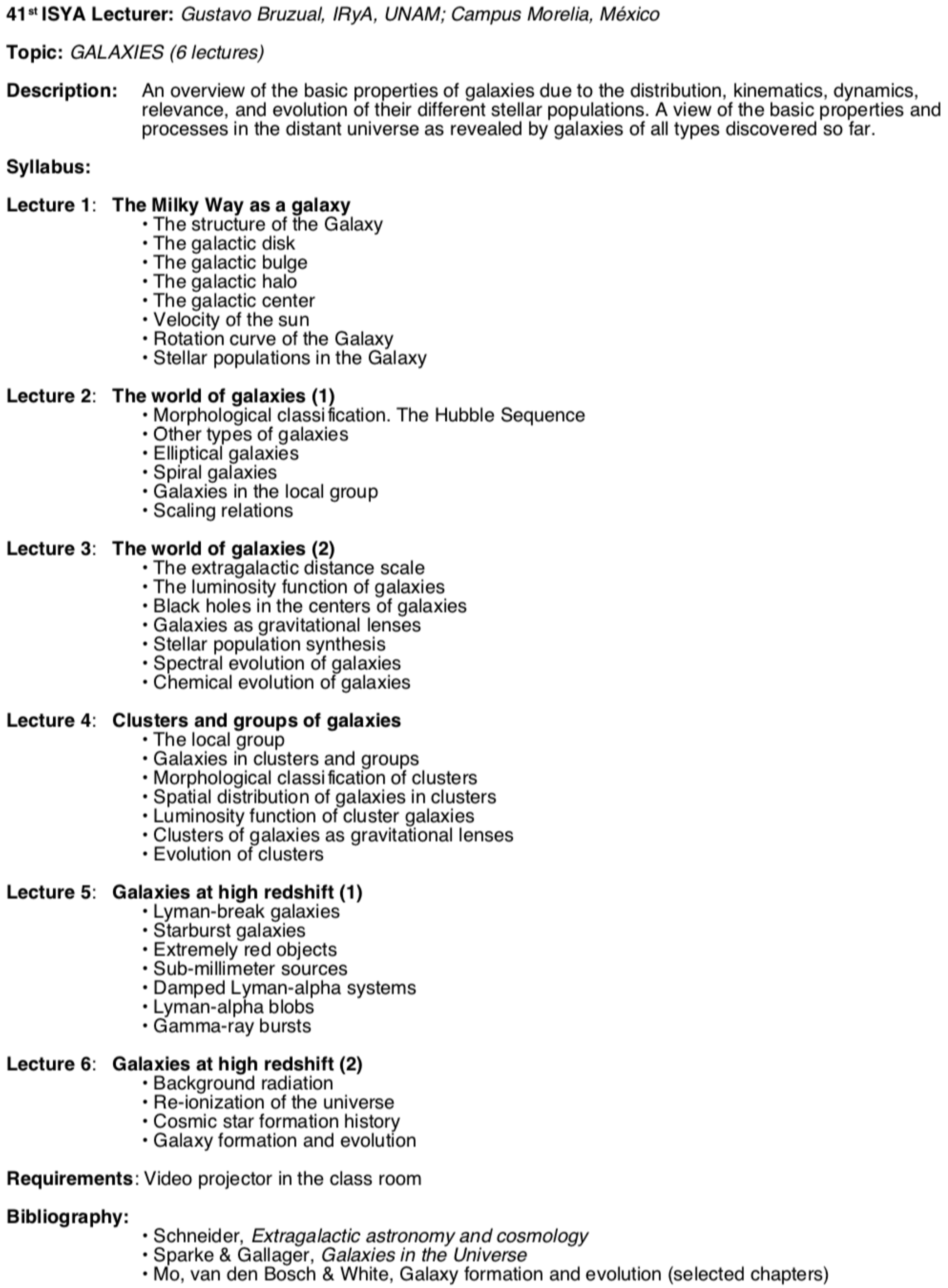

41st ISYA Lecturer: *Gustavo Bruzual, IRyA, UNAM; Campus Morelia, México*

Topic: *GALAXIES (6 lectures)*

Description: An overview of the basic properties of galaxies due to the distribution, kinematics, dynamics, relevance, and evolution of their different stellar populations. A view of the basic properties and processes in the distant universe as revealed by galaxies of all types discovered so far.

Syllabus:

Lecture 1: The Milky Way as a galaxy
- The structure of the Galaxy
- The galactic disk
- The galactic bulge
- The galactic halo
- The galactic center
- Velocity of the sun
- Rotation curve of the Galaxy
- Stellar populations in the Galaxy

Lecture 2: The world of galaxies (1)
- Morphological classification. The Hubble Sequence
- Other types of galaxies
- Elliptical galaxies
- Spiral galaxies
- Galaxies in the local group
- Scaling relations

Lecture 3: The world of galaxies (2)
- The extragalactic distance scale
- The luminosity function of galaxies
- Black holes in the centers of galaxies
- Galaxies as gravitational lenses
- Stellar population synthesis
- Spectral evolution of galaxies
- Chemical evolution of galaxies

Lecture 4: Clusters and groups of galaxies
- The local group
- Galaxies in clusters and groups
- Morphological classification of clusters
- Spatial distribution of galaxies in clusters
- Luminosity function of cluster galaxies
- Clusters of galaxies as gravitational lenses
- Evolution of clusters

Lecture 5: Galaxies at high redshift (1)
- Lyman-break galaxies
- Starburst galaxies
- Extremely red objects
- Sub-millimeter sources
- Damped Lyman-alpha systems
- Lyman-alpha blobs
- Gamma-ray bursts

Lecture 6: Galaxies at high redshift (2)
- Background radiation
- Re-ionization of the universe
- Cosmic star formation history
- Galaxy formation and evolution

Requirements: Video projector in the class room

Bibliography:
- Schneider, *Extragalactic astronomy and cosmology*
- Sparke & Gallager, *Galaxies in the Universe*
- Mo, van den Bosch & White, Galaxy formation and evolution (selected chapters)

The Universe at High Redshift

We want to understand how the Universe evolved from a very primitive initial state into what we are observing around us today – galaxies of different morphologies, the large-scale structure of their distribution, clusters of galaxies, and active galaxies. We seek to study the formation of stars and of metals, and also the processes that reionized the intergalactic medium.

The boundary conditions for studying these processes are now very well defined. A few years ago, the cosmological parameters in models of galaxy evolution, for instance, could vary freely because they had not been determined sufficiently well at that time. Today, a successful model needs to come up with predictions compatible with observations, but using the parameters of the standard model. There is little freedom left in designing such models. In other words, the stage on which the formation and evolution of objects and structure takes place is prepared, and now the cosmic play can begin.

Progress in recent years, with developments in instrumentation having played a vital role, has allowed us to examine the Universe at very high redshift. An obvious indication of this progress is the increasingly high maximum redshift of sources that can be observed; as an example, Fig. 9.1 presents the spectrum of a QSO at redshift $z = 6.43$. Today, we know quite a few galaxies at redshift $z > 6$, i.e., we observe these objects at a time when the Universe had less than 10% of its current age.

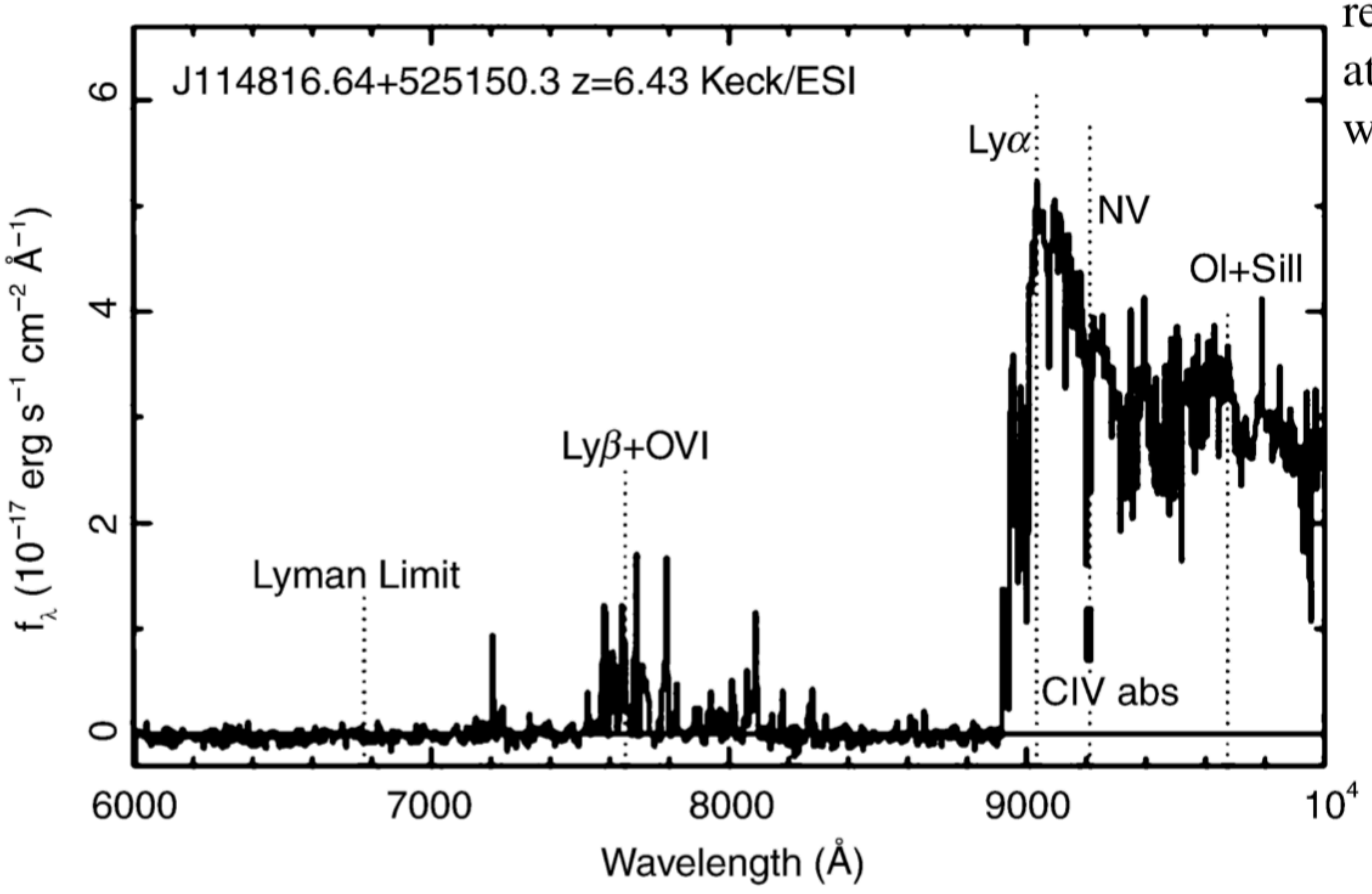

Fig. 9.1. Spectrum of a QSO at the high redshift of $z = 6.43$. Like many other QSOs at very high redshift, this source was discovered with the Sloan Digital Sky Survey. The spectrum was obtained with the Keck telescope. The redshifted Lyα line is clearly visible, its blue side "eaten" away by intergalactic absorption. Almost all radiation bluewards of the Lyα line is absorbed, with only the emission from the Lyβ line still getting through. For $\lambda \leq 7200$ Å the spectral flux is compatible with zero; intergalactic absorption is too strong here

Galaxies at High Redshift

Lyman-Break Galaxies (LBGs)

The Lyman-Break Method. The breakthrough was obtained with a method that became known as the *Lyman-break method*. Since hydrogen is so abundant and its ionization cross-section so large, one can expect that photons with $\lambda < 912$ Å are very heavily absorbed by neutral hydrogen in its ground state. Therefore, photons with $\lambda < 912$ Å have a low probability of escaping from a galaxy without being absorbed.

Intergalactic absorption also contributes. In Sect. 5.6.3 we saw that each QSO spectrum features a Lyα forest and Lyman-limit absorption. The intergalactic gas absorbs a large fraction of photons emitted by a high-redshift source at $\lambda < 1216$ Å, and virtually all photons with a rest-frame wavelength $\lambda \lesssim 912$ Å. As also discussed in Sect. 8.5.2, the strength of this absorption increases with increasing redshift. Combining these facts, we conclude that spectra of high-redshift galaxies should display a distinct feature – a "break" – at $\lambda = 1216$ Å. Furthermore, radiation with $\lambda \lesssim 912$ Å should be strongly suppressed by intergalactic absorption, as well as by absorption in the interstellar medium of the galaxies themselves, so that only a very small fraction of these ionizing photons will reach us.

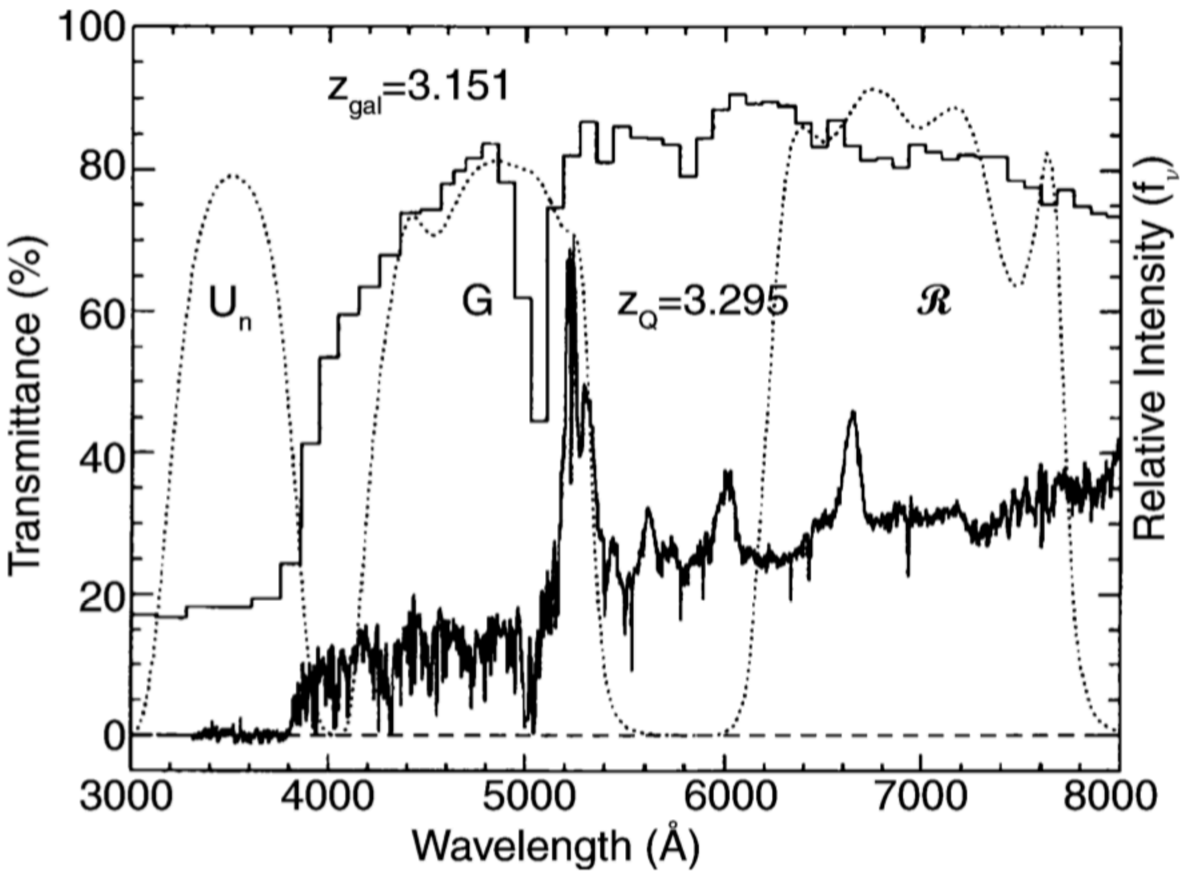

Fig. 9.2. Principle of the Lyman-break method. The histogram shows the synthetic spectrum of a galaxy at $z = 3.15$, generated by models of population synthesis; the spectrum belongs to a QSO at slightly higher redshift. Clearly, the decline of the spectrum at $\lambda \le 912(1+z)$Å is noticeable. The three dotted curves are the transmission curves of three broad-band filters, chosen such that one of them ($\mathrm{U_n}$) blocks all photons with wavelengths above the Lyman-break. The color of this galaxy would then be blue in $\mathrm{G} - \mathcal{R}$, and very red in $\mathrm{U_n} - \mathrm{G}$

From this, a strategy for the detection of galaxies at $z \gtrsim 3$ emerges. We consider three broad-band filters with central wavelengths $\lambda_1 < \lambda_2 < \lambda_3$, where their spectral ranges are chosen to not (or only marginally) overlap. If $\lambda_1 \lesssim (1+z)\,912$ Å $\lesssim \lambda_2$, a galaxy containing young stars should appear relatively blue as measured with the filters λ_2 and λ_3, and be virtually invisible in the λ_1-filter: because of the absorption, it will drop out of the λ_1-filter (see Fig. 9.2). For this reason, galaxies that have been detected in this way are called *Lyman-break galaxies* (LBG) or *drop-outs*. An example of this is displayed in Fig. 9.3.

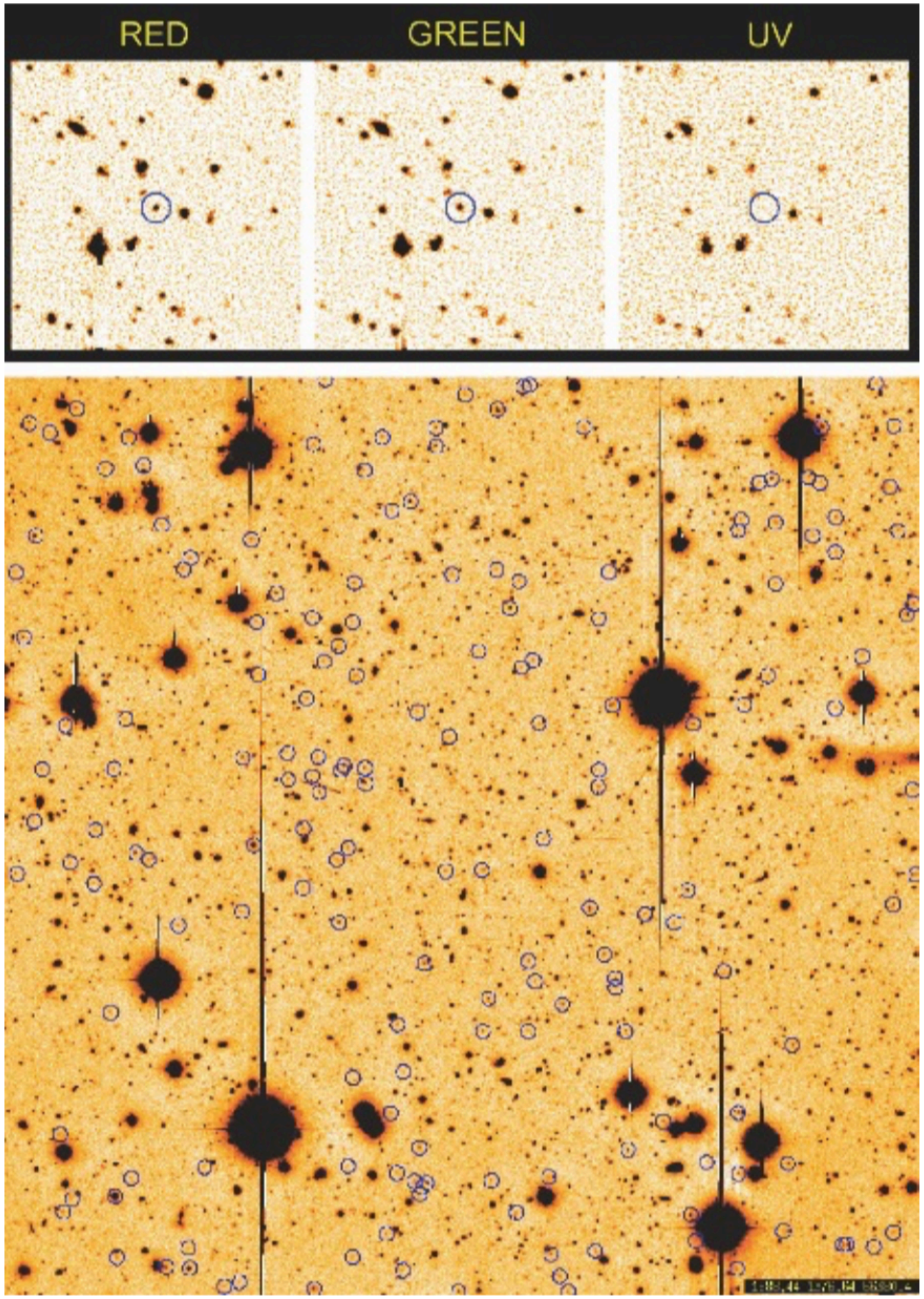

Fig. 9.3. Top panel: a U-band drop-out galaxy. It is clearly detected in the two redder filters, but vanishes almost completely in the U-filter. Bottom panel: in a single CCD frame, a large number of candidate Lyman-break galaxies are found. They are marked with circles here; their density is about 1 per square arcminute

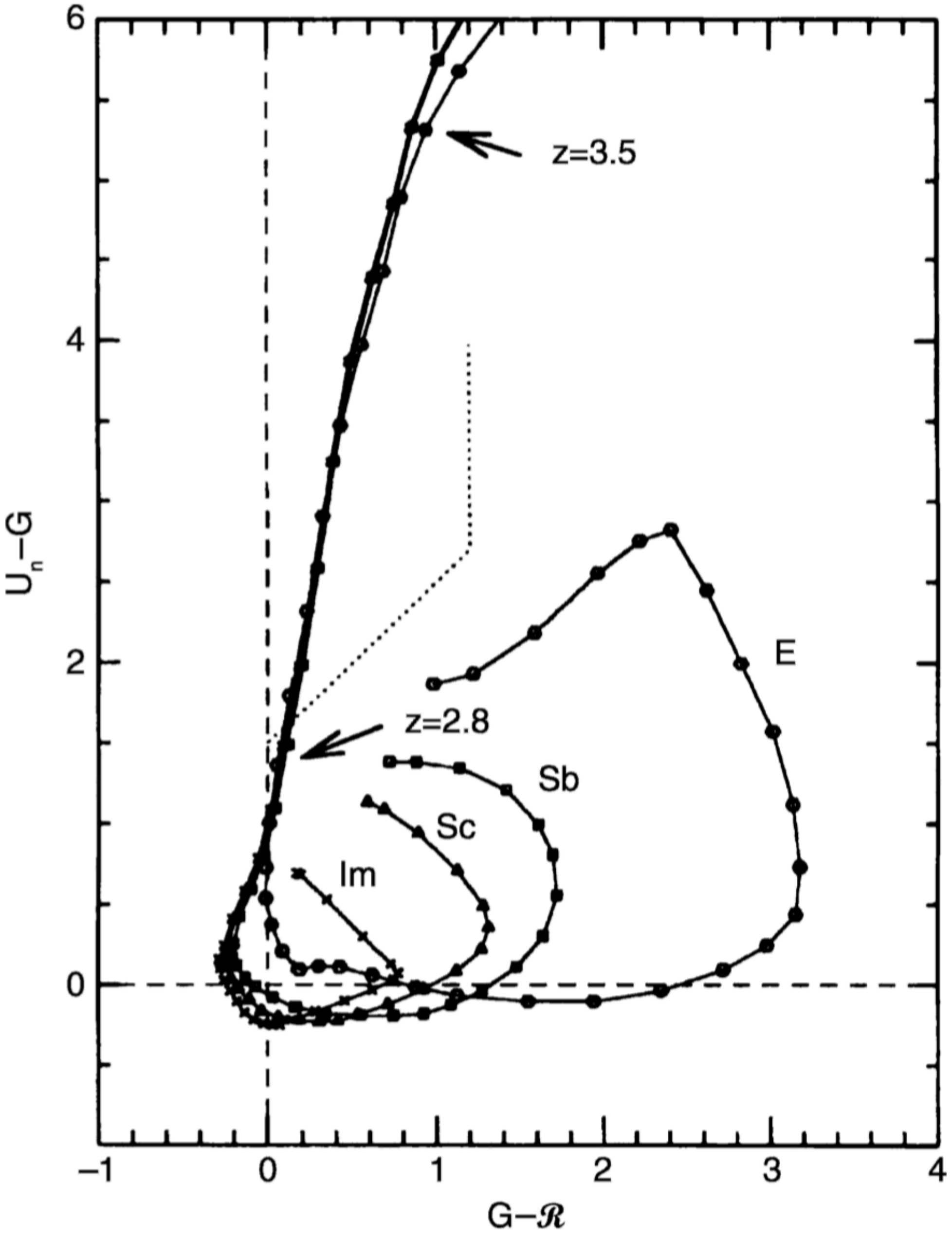

Fig. 9.4. Evolutionary tracks of galaxies in the $(G-\mathcal{R})$ – (U_n-G) color–color diagram, for different types of galaxies, as obtained from population synthesis models. All evolutionary tracks start at $z=0$, and the symbols along the curves mark intervals of $\Delta z=0.1$. The colors of the various galaxy types are very different at lower redshift, but for $z \geq 2.7$, the evolutionary tracks for the different types nearly coincide – a consequence of the Lyα absorption in the intergalactic medium. Hence, a color selection of galaxies in the region between the dotted and dashed curves should select galaxies with $z \geq 3$. Indeed, this selection of candidates has proven to be very successful; more than 1000 galaxies with $z \sim 3$ have been spectroscopically verified

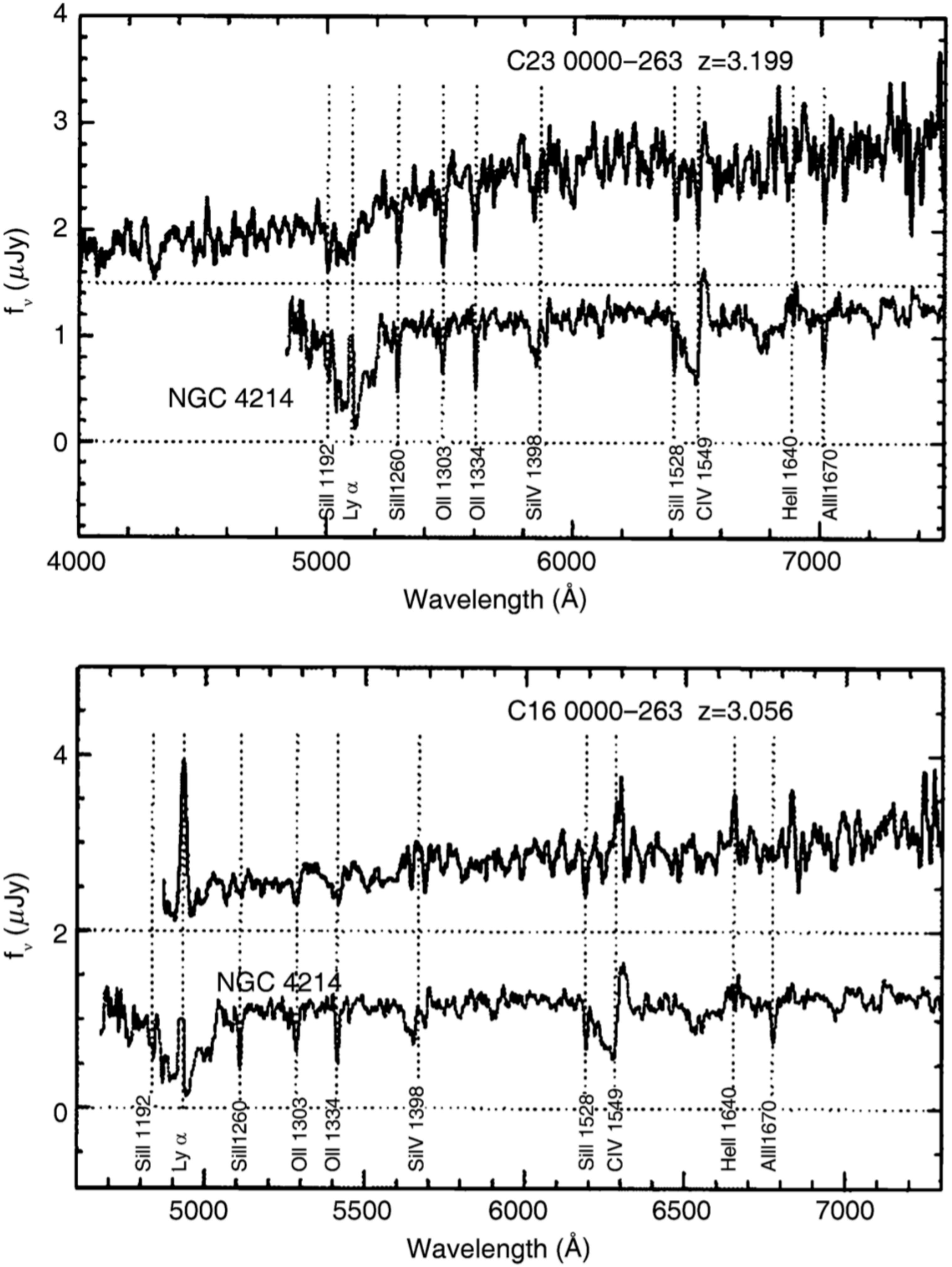

Fig. 9.5. Spectra of two galaxies at $z \sim 3$, detected by means of the U-drop-out technique. Below each spectrum, the spectrum of a nearby starburst galaxy (NGC 4214) – shifted to the corresponding redshift – is plotted; it becomes apparent that the spectra of galaxies at $z \sim 3$ are very similar to those of present-day galaxies. One of the two U-drop-out galaxies features a strong Lyα emission line, the other shows absorption at the respective wavelength

From the spectra shown in Fig. 9.5, it also becomes apparent that not all galaxies which fulfill the selection criteria also show a Lyα emission line, which provides one possible explanation for the lack of success in earlier searches for high-redshift galaxies using narrow-band filters. The spectra of the high-redshift galaxies which were found by this method are very similar to those of starburst galaxies at low redshift. Obviously, the galaxies selected in this way feature active star formation. Due to the chosen selection criterion, such sources are, of course, preferentially selected, since star formation produces a blue spectrum at (rest-frame) wavelengths above 1216 Å; in addition the luminosity of galaxies in the UV range strongly depends on the star-formation rate.

Connection to QSO Absorption Lines. A slightly more indirect argument for the presence of strong winds from LBGs comes from correlating the absorption lines in background QSO spectra with the position of LBGs. These studies have shown that whenever the sightline of a QSO passes within $\sim 40\,\mathrm{kpc}$ of an LBG, very strong C IV absorption lines (with column density exceeding $10^{14}\,\mathrm{cm}^{-2}$) are produced, and that the corresponding absorbing material spans a velocity range of $\Delta v \gtrsim 250\,\mathrm{km/s}$; for about half of the cases, strong C IV absorption is produced for impact parameters within 80 kpc. This frequency of occurrence implies that about $1/3$ of all C IV metal absorption lines with $N \gtrsim 10^{14}\,\mathrm{cm}^{-2}$ in QSO spectra are due to gas within $\sim 80\,\mathrm{kpc}$ from those LBGs which are bright enough to be included in current surveys. It is plausible that the remaining $2/3$ are due to fainter LBGs.

Finally, we mention another piece of evidence for the presence of superwinds in star-forming galaxies. There are indications that the density of absorption lines in the Lyα forest is reduced when the sightline to the QSO passes near a foreground LBG. This may well be explained by a wind driven out from the LBG, pushing neutral gas away and thus leaving a gap in the Lyα forest. The characteristic size of the corresponding "bubbles" is $\sim 0.5\,\mathrm{Mpc}$ for luminous LBGs.

Lyman-Break Galaxies at Low Redshifts. One might ask whether galaxies similar to the LBGs at $z \sim 3$ exist in the current Universe. Until recently this question was difficult to investigate, since it requires imaging of lower redshift galaxies at ultraviolet wavelengths. With the launch of GALEX an appropriate observatory became available with which to observe galaxies with rest-frame UV luminosities similar to those of LBGs. UV-selected galaxies show a strong inverse correlation between the stellar mass and the surface brightness in the UV. Lower-mass galaxies are more compact than those of higher stellar mass. On the basis of this correlation we can consider the population of large and compact UV-selected galaxies separately. The larger ones show a star-formation rate of a few $M_\odot/\mathrm{yr}$; at this rate, their stellar mass content can be built up on a time-scale comparable to the Hubble time, i.e., the age of the Universe. These galaxies are typically late-type spiral galaxies, and they show a metallicity similar to our Galaxy. In contrast, the compact galaxies have a lower stellar mass and about the same star-formation rate, which allows them to generate their stellar population much faster, in about 1 Gyr. Their metallicity is smaller by about a factor of 2. These properties of these compact UV-selected galaxies are quite similar to those of the LBGs seen at higher redshifts, and hence, they may be closely related to the LBG population.

Lyman-Break Galaxies at High Redshift. By variation of the filter set, drop-outs can also be discovered at larger wavelengths, thus at accordingly higher redshifts. The object selection at higher z implies an increasingly dominant role of the Lyα forest whose density is a strongly increasing function of redshift (see Sect. 8.5.2). This method has been routinely applied up to $z \sim 4.5$, yielding so-called B-drop-outs. Galaxies at considerably higher redshifts are difficult to access from the ground with this method. One reason for this is that galaxies become increasingly faint with redshift, rendering observations substantially more problematic. Furthermore, one needs to use increasingly redder filter sets. At such large wavelengths the night sky gets significantly brighter, which further hampers the detection of very faint objects. For detecting a galaxy at redshift, say, $z = 5.5$ with this method, the Lyα line, now at $\lambda \approx 7900$ Å, is located right in the I-band, so that for an efficient application of the drop-out technique only the I- and z-band filters or NIR-filters are viable, and with those filters the brightness of the night sky is very problematic (see Fig. 9.6 for an example of a drop-out galaxy at very high redshift). Furthermore, candidate very high-redshift galaxies detected as drop-outs are very difficult to verify spectroscopically due to their very low flux.]

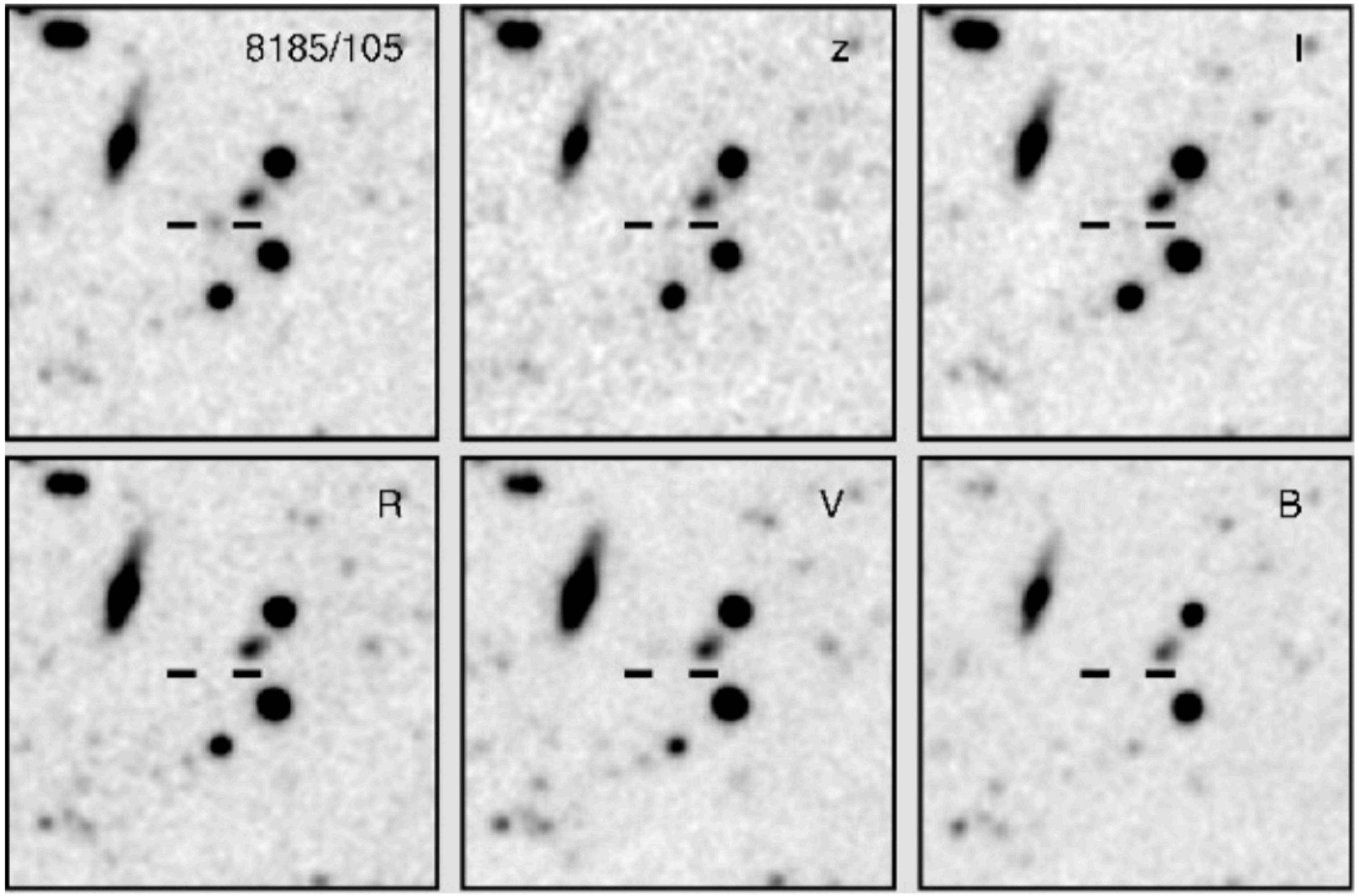

Fig. 9.6. A galaxy at $z = 5.74$, which is visible in the narrow-band filter (upper left panel) and in the I- and z-band (located between the two horizontal dashes), but which does not show any flux in the three filters at shorter wavelength

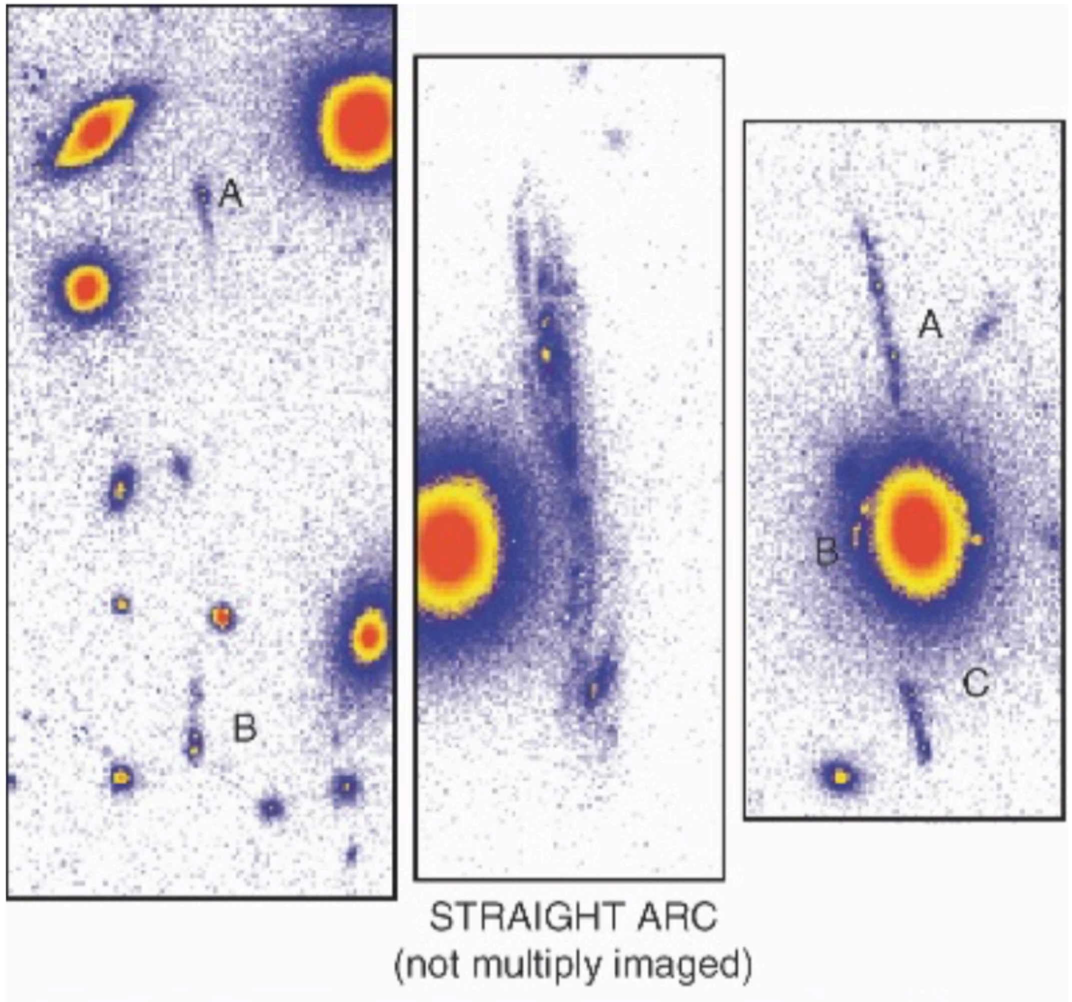

Fig. 9.12. A particularly interesting and efficient way to examine galaxies at high redshift is provided by the strong lensing effect in clusters of galaxies. Since a gravitational lens can magnify the light of background galaxies (by magnification of the solid angle), one can expect to detect apparently brighter galaxies at high redshift in the background of clusters. Here, an HST image of the cluster Abell 2390 is shown, in which several lens systems are visible. On the left, the central region of the cluster is shown. Three systems with a strong lens effect in this cluster are presented in the blow-ups at top. In the center, the so-called "straight arc" is visible which has a redshift of about 0.91. On the right and left, two multiply imaged systems are displayed, the images indicated by letters; the two sources associated with these images have redshifts of $z = 4.04$ and 4.05, respectively

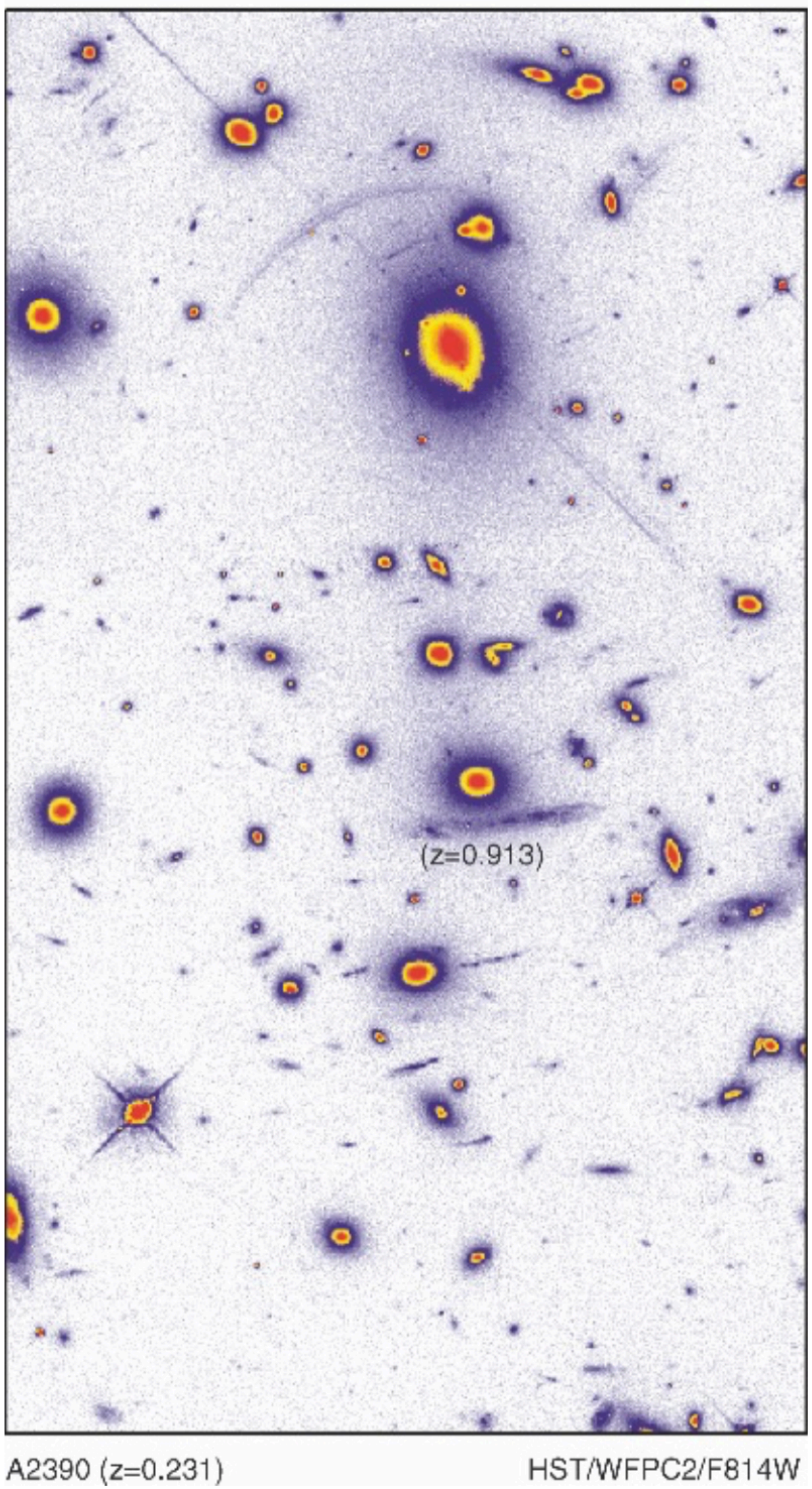

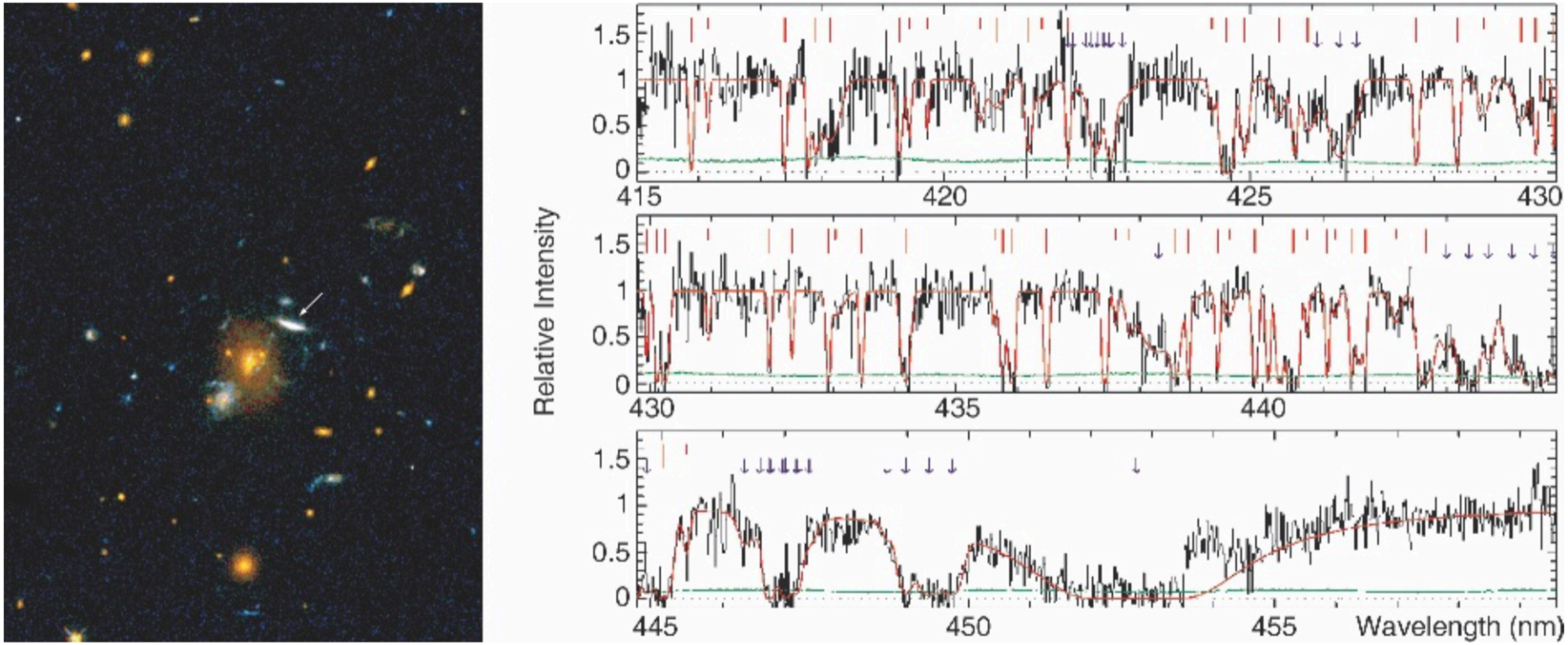

Fig. 9.13. The image on the left was taken by the Hubble Space Telescope. It shows the cluster of galaxies MS1512+36, which has a redshift of $z = 0.37$. To the right, and slightly above the central cluster galaxy, an extended and apparently very blue object is seen, marked by an arrow. This source is not physically associated with the cluster but is a background galaxy at a redshift of $z = 2.72$. With this HST image it was proved that this galaxy is strongly lensed by the cluster and, by means of this, magnified by a factor of ~ 30. Due to the magnification, this Lyman-break galaxy is the brightest normal galaxy at redshift $z \sim 3$, a fact that can be profitably used for a detailed spectroscopic analysis. On the right, a small section from a high-resolution VLT spectrum of this galaxy is shown. The Lyα transition of the galaxy is located at $\lambda = 4530\,\text{Å}$, visible as a broad absorption line. Absorption lines at shorter wavelengths originate from the Lyα-forest along the line-of-sight (indicated by short vertical lines) or by metal lines from the galaxy itself (indicated by arrows)

Starburst Galaxies

True Optical colors Hα

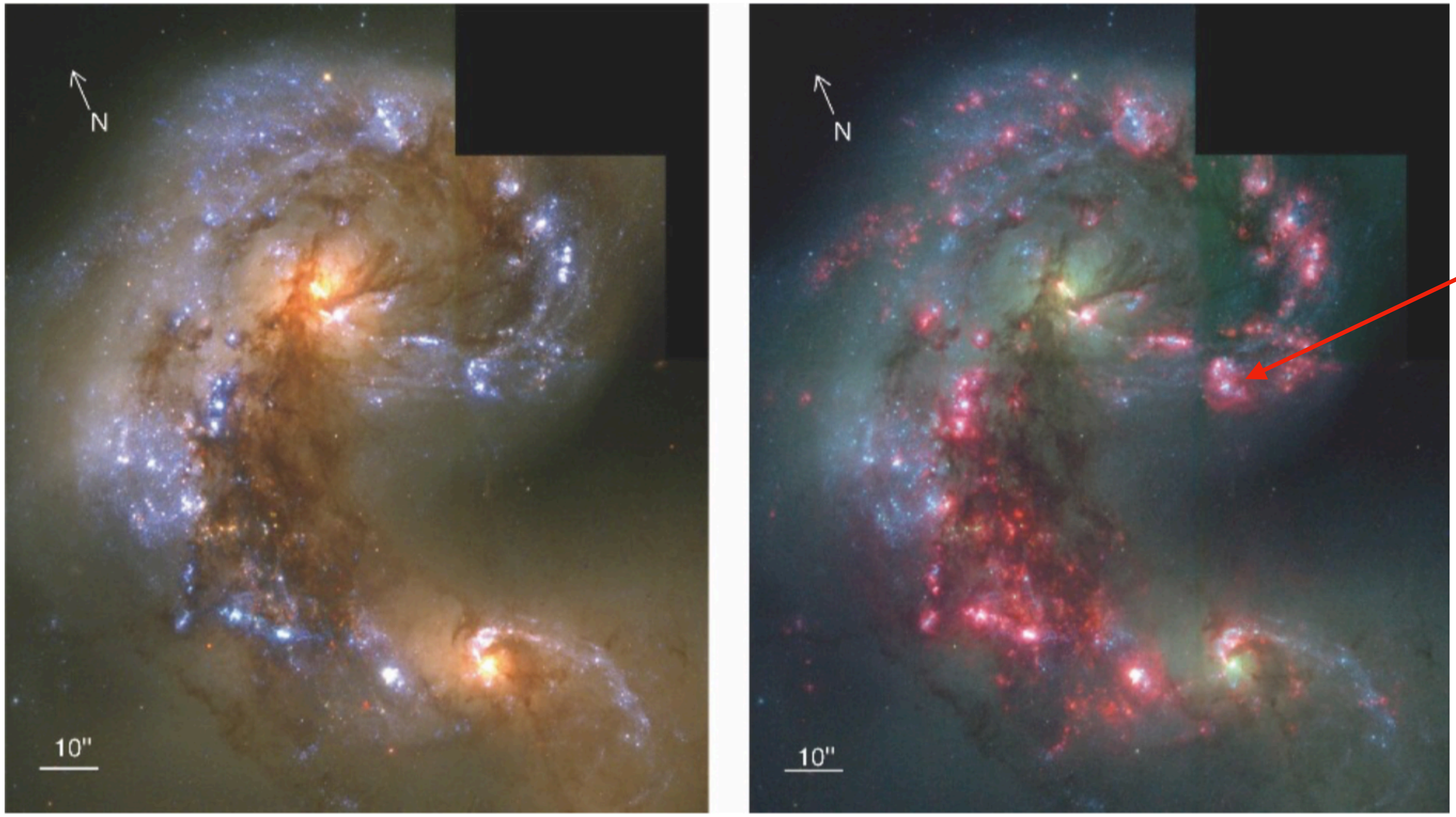

10^5 $M_\odot$

star clusters

Fig. 9.15. The Antenna galaxies. On the left, the "true" optical colors are shown, whereas in the right-hand image the reddish color shows Hα emission. This pair of merging galaxies (also see Fig. 1.13 and Fig. 3.4 for other examples of merging galaxies) is forming an enormous number of young stars. Both the UV emission (bluish in the left image) and the Hα radiation (reddish in the right image) are considered indicators of star formation. The individual knots of bright emission are not single stars but star clusters with typically $10^5 M_\odot$; however, it is also possible to resolve individual stars (red and blue supergiants) in these galaxies

Antenna Galaxies

Starburst Galaxies

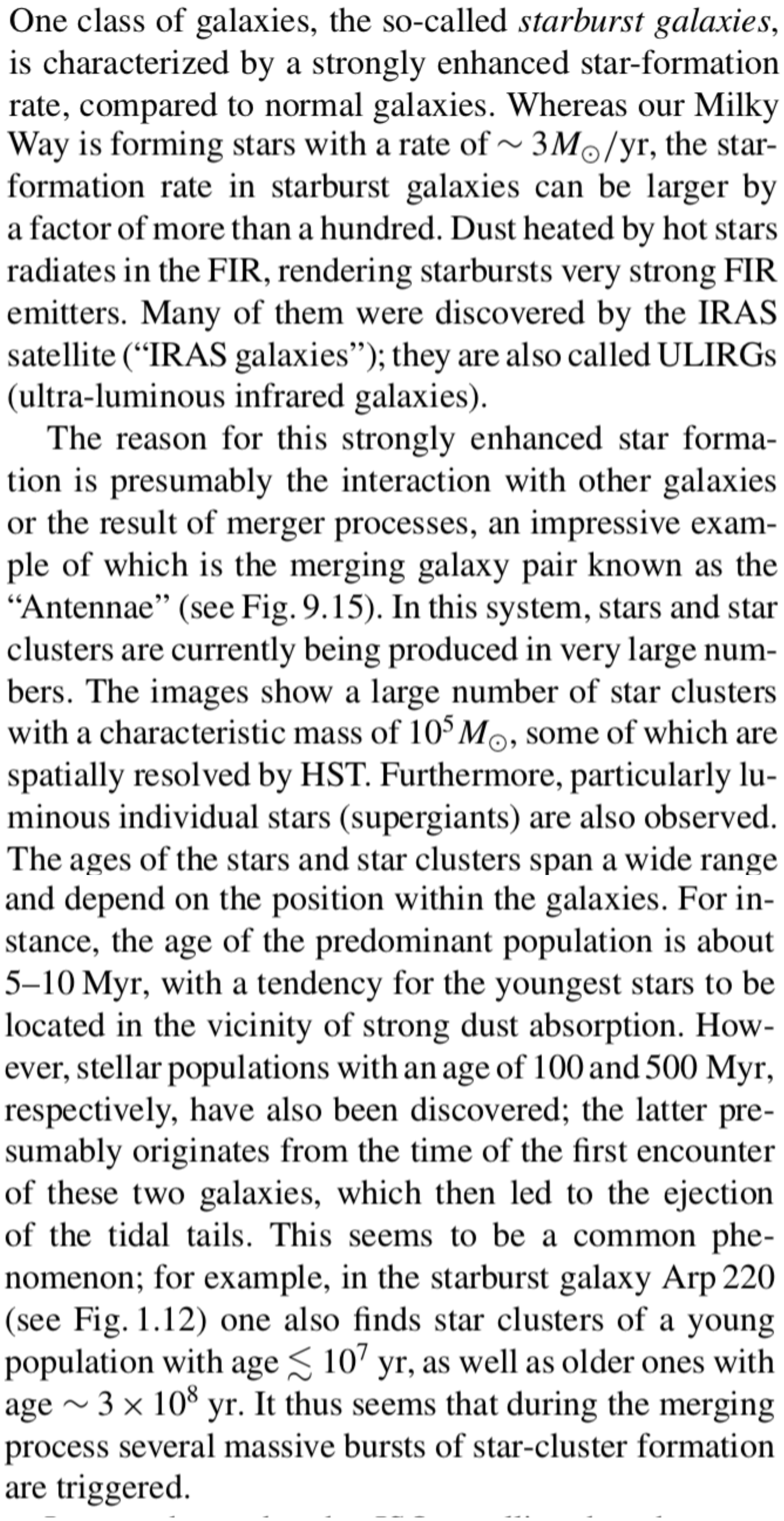

One class of galaxies, the so-called *starburst galaxies*, is characterized by a strongly enhanced star-formation rate, compared to normal galaxies. Whereas our Milky Way is forming stars with a rate of $\sim 3 M_\odot/\mathrm{yr}$, the star-formation rate in starburst galaxies can be larger by a factor of more than a hundred. Dust heated by hot stars radiates in the FIR, rendering starbursts very strong FIR emitters. Many of them were discovered by the IRAS satellite ("IRAS galaxies"); they are also called ULIRGs (ultra-luminous infrared galaxies).

The reason for this strongly enhanced star formation is presumably the interaction with other galaxies or the result of merger processes, an impressive example of which is the merging galaxy pair known as the "Antennae" (see Fig. 9.15). In this system, stars and star clusters are currently being produced in very large numbers. The images show a large number of star clusters with a characteristic mass of $10^5 M_\odot$, some of which are spatially resolved by HST. Furthermore, particularly luminous individual stars (supergiants) are also observed. The ages of the stars and star clusters span a wide range and depend on the position within the galaxies. For instance, the age of the predominant population is about 5–10 Myr, with a tendency for the youngest stars to be located in the vicinity of strong dust absorption. However, stellar populations with an age of 100 and 500 Myr, respectively, have also been discovered; the latter presumably originates from the time of the first encounter of these two galaxies, which then led to the ejection of the tidal tails. This seems to be a common phenomenon; for example, in the starburst galaxy Arp 220 (see Fig. 1.12) one also finds star clusters of a young population with age $\lesssim 10^7$ yr, as well as older ones with age $\sim 3 \times 10^8$ yr. It thus seems that during the merging process several massive bursts of star-cluster formation are triggered.

enhanced SF

IRAS galaxies
ULIRGs

Arp 220

Fig. 1.12. Arp 220 is the most luminous object in the local Universe. Originally cataloged as a peculiar galaxy, the infrared satellite IRAS later discovered its enormous luminosity in the infrared (IR). Arp 220 is the prototype of ultra-luminous infrared galaxies (ULIRGs). This near-IR image taken with the Hubble Space Telescope (HST) unveils the structure of this object. With two colliding spiral galaxies in the center of Arp 220, the disturbances in the interstellar medium caused by this collision trigger a starburst. Dust in the galaxy absorbs most of the ultraviolet (UV) radiation from the young hot stars and re-emits it in the IR

Starburst Galaxies

IR emission at 1.5 μm

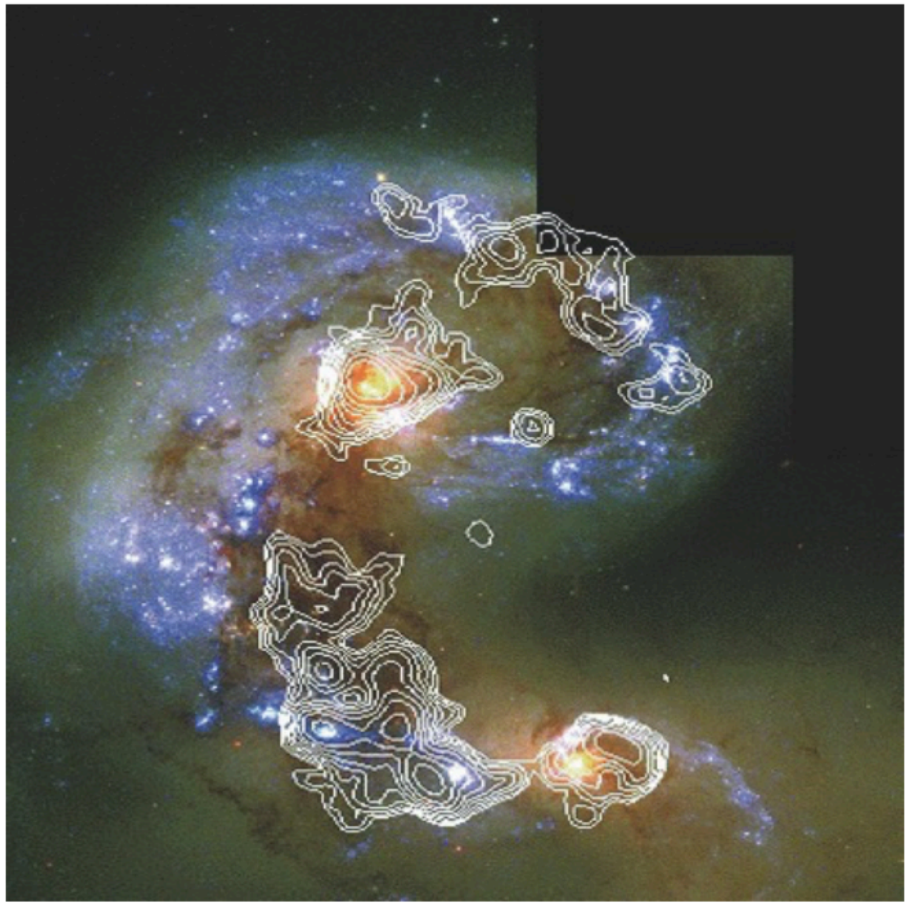

Fig. 9.16. The Antenna galaxies: superposed on the optical HST image are contours of infrared emission at 15 μm, measured by ISO. The strongest IR emission originates in optically dark regions. A large fraction of the star formation in this galaxy pair (and in other galaxies?) is not visible on optical images because it is hidden by dust absorption

True Optical colors

Hα

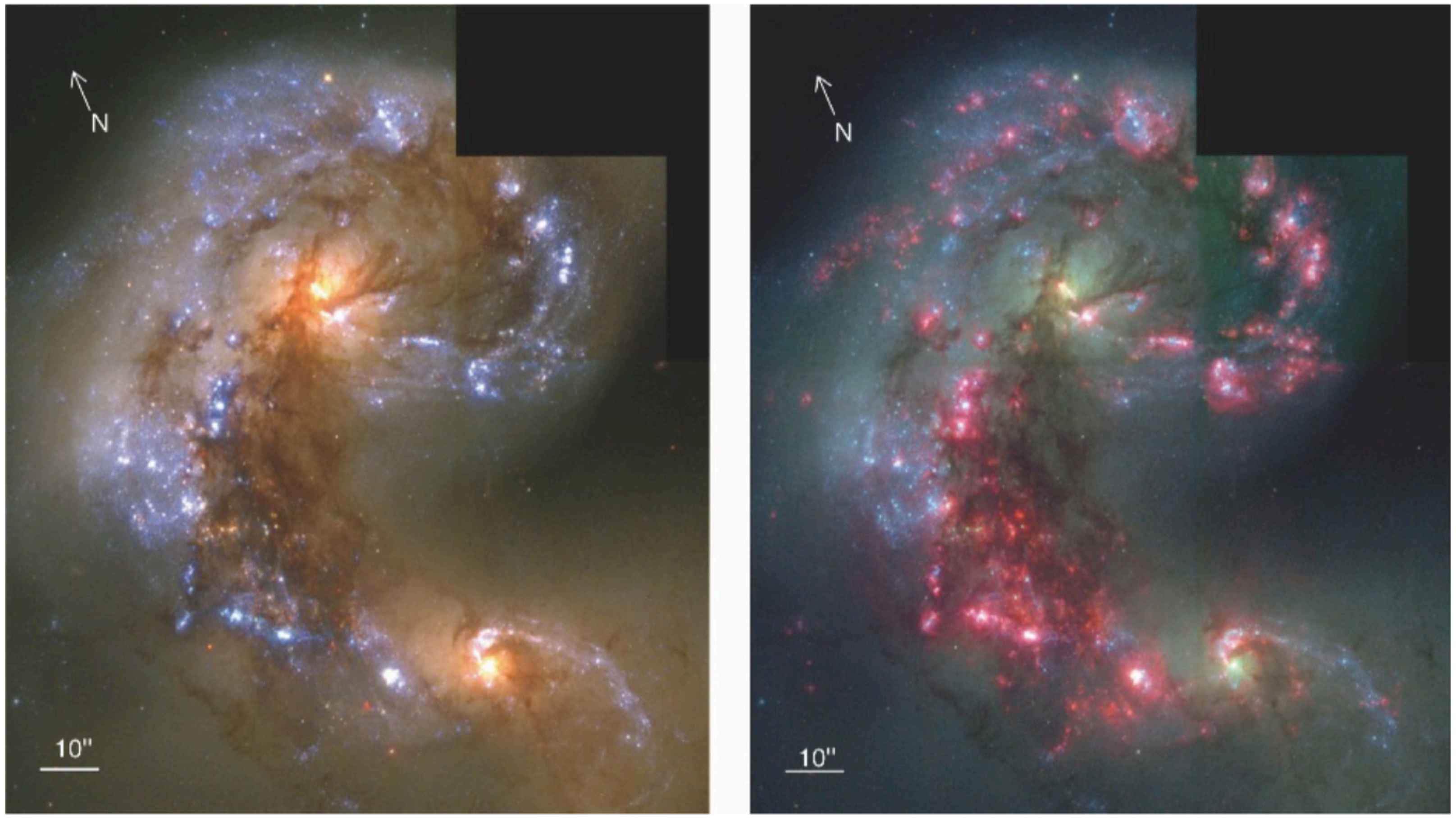

Fig. 9.15. The Antenna galaxies. On the left, the "true" optical colors are shown, whereas in the right-hand image the reddish color shows Hα emission. This pair of merging galaxies (also see Fig. 1.13 and Fig. 3.4 for other examples of merging galaxies) is forming an enormous number of young stars. Both the UV emission (bluish in the left image) and the Hα radiation (reddish in the right image) are considered indicators of star formation. The individual knots of bright emission are not single stars but star clusters with typically $10^5 M_\odot$; however, it is also possible to resolve individual stars (red and blue supergiants) in these galaxies

Antenna Galaxies

Starburst Galaxies

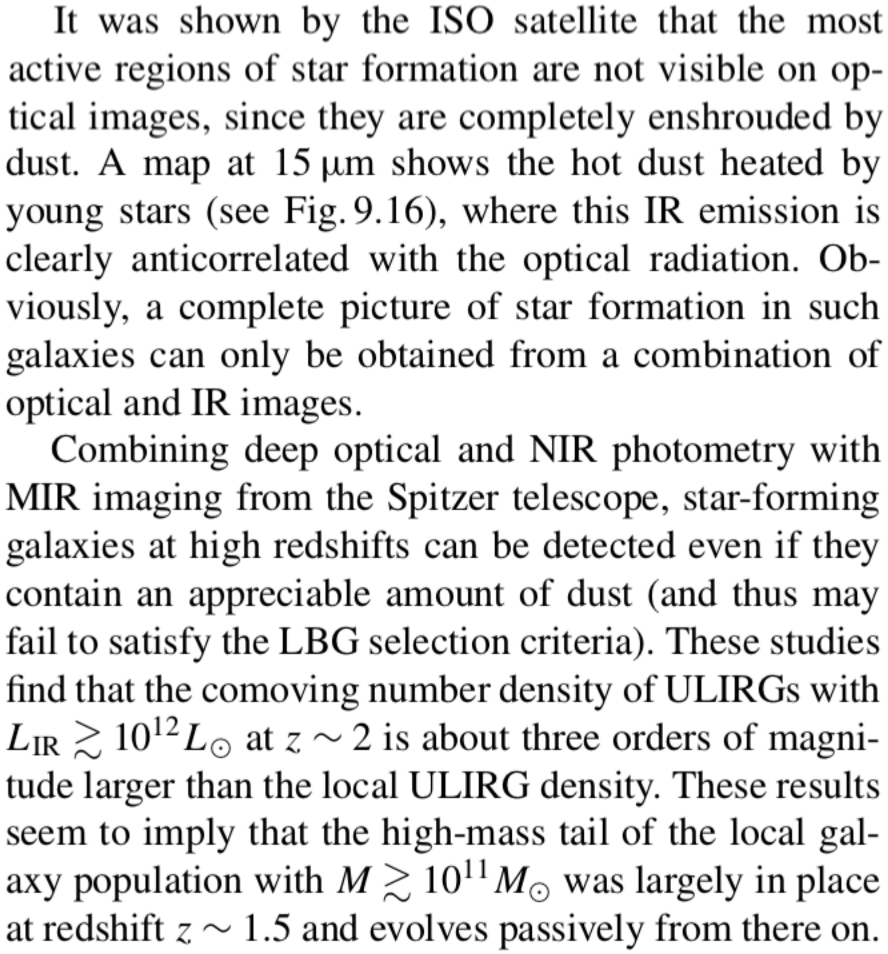

It was shown by the ISO satellite that the most active regions of star formation are not visible on optical images, since they are completely enshrouded by dust. A map at 15 µm shows the hot dust heated by young stars (see Fig. 9.16), where this IR emission is clearly anticorrelated with the optical radiation. Obviously, a complete picture of star formation in such galaxies can only be obtained from a combination of optical and IR images.

Combining deep optical and NIR photometry with MIR imaging from the Spitzer telescope, star-forming galaxies at high redshifts can be detected even if they contain an appreciable amount of dust (and thus may fail to satisfy the LBG selection criteria). These studies find that the comoving number density of ULIRGs with $L_{\rm IR} \gtrsim 10^{12} L_\odot$ at $z \sim 2$ is about three orders of magnitude larger than the local ULIRG density. These results seem to imply that the high-mass tail of the local galaxy population with $M \gtrsim 10^{11} M_\odot$ was largely in place at redshift $z \sim 1.5$ and evolves passively from there on.

IR emission at 1.5 μm

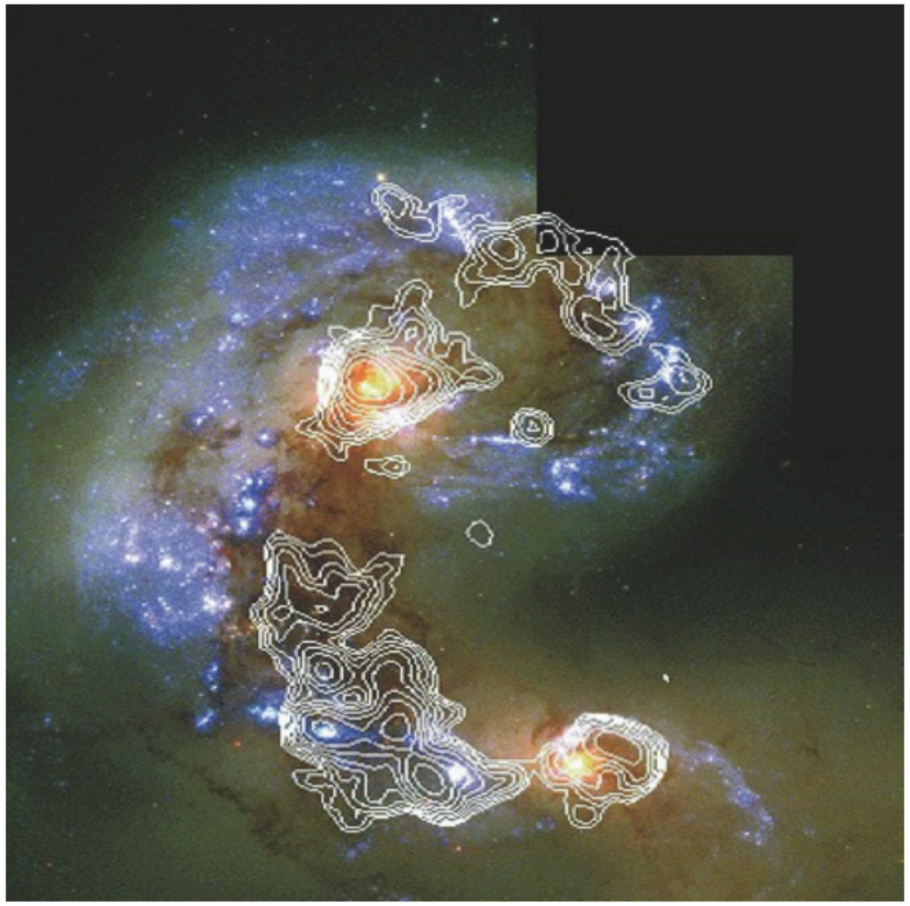

Fig. 9.16. The Antenna galaxies: superposed on the optical HST image are contours of infrared emission at 15 µm, measured by ISO. The strongest IR emission originates in optically dark regions. A large fraction of the star formation in this galaxy pair (and in other galaxies?) is not visible on optical images because it is hidden by dust absorption

Starburst Galaxies

IR emission at 1.5 μm

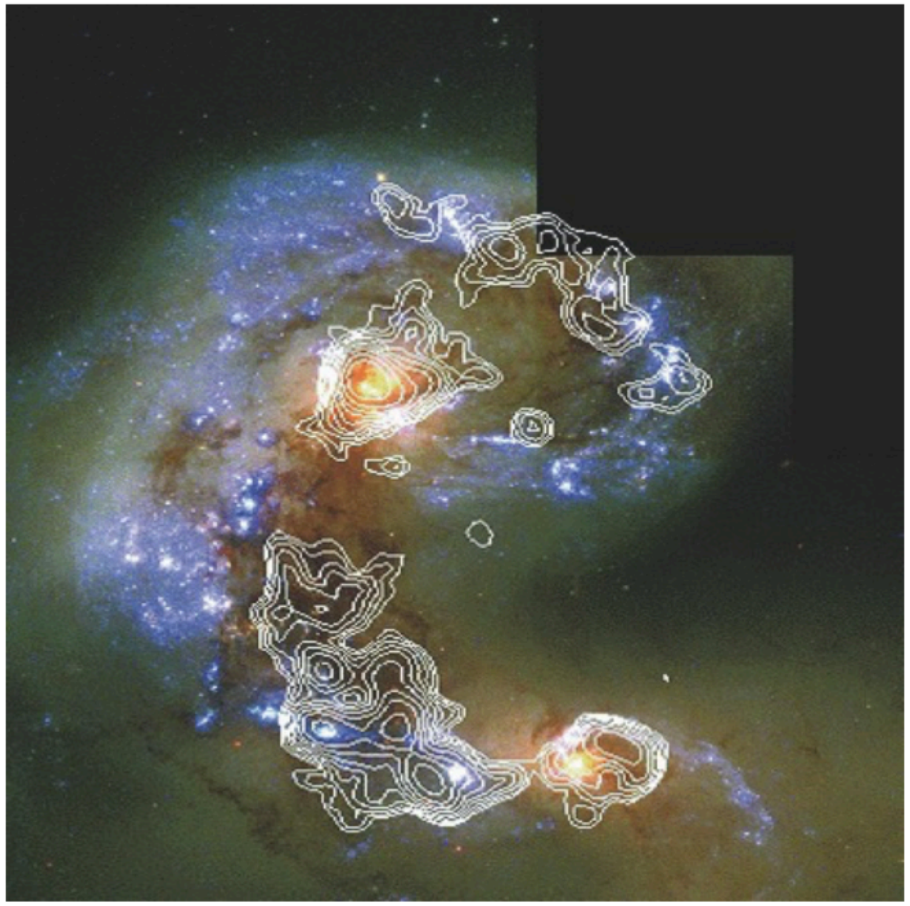

Fig. 9.16. The Antenna galaxies: superposed on the optical HST image are contours of infrared emission at 15 µm, measured by ISO. The strongest IR emission originates in optically dark regions. A large fraction of the star formation in this galaxy pair (and in other galaxies?) is not visible on optical images because it is hidden by dust absorption

Discrete X-ray sources (ULXs)

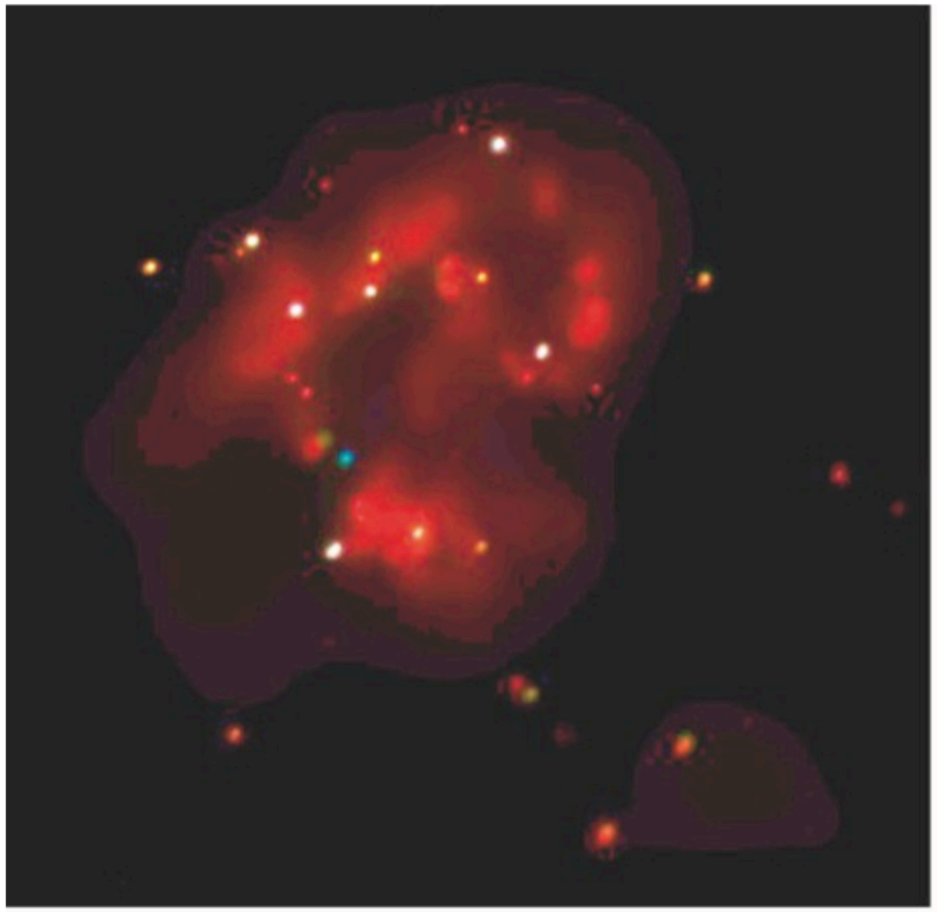

Fig. 9.17. Ultra-luminous Compact X-ray Sources (ULXs) in starburst galaxies. Upper left: the discrete X-ray sources in the Antenna galaxies; the size of the image is $4' \times 4'$.

Antenna Galaxies

Starburst Galaxies

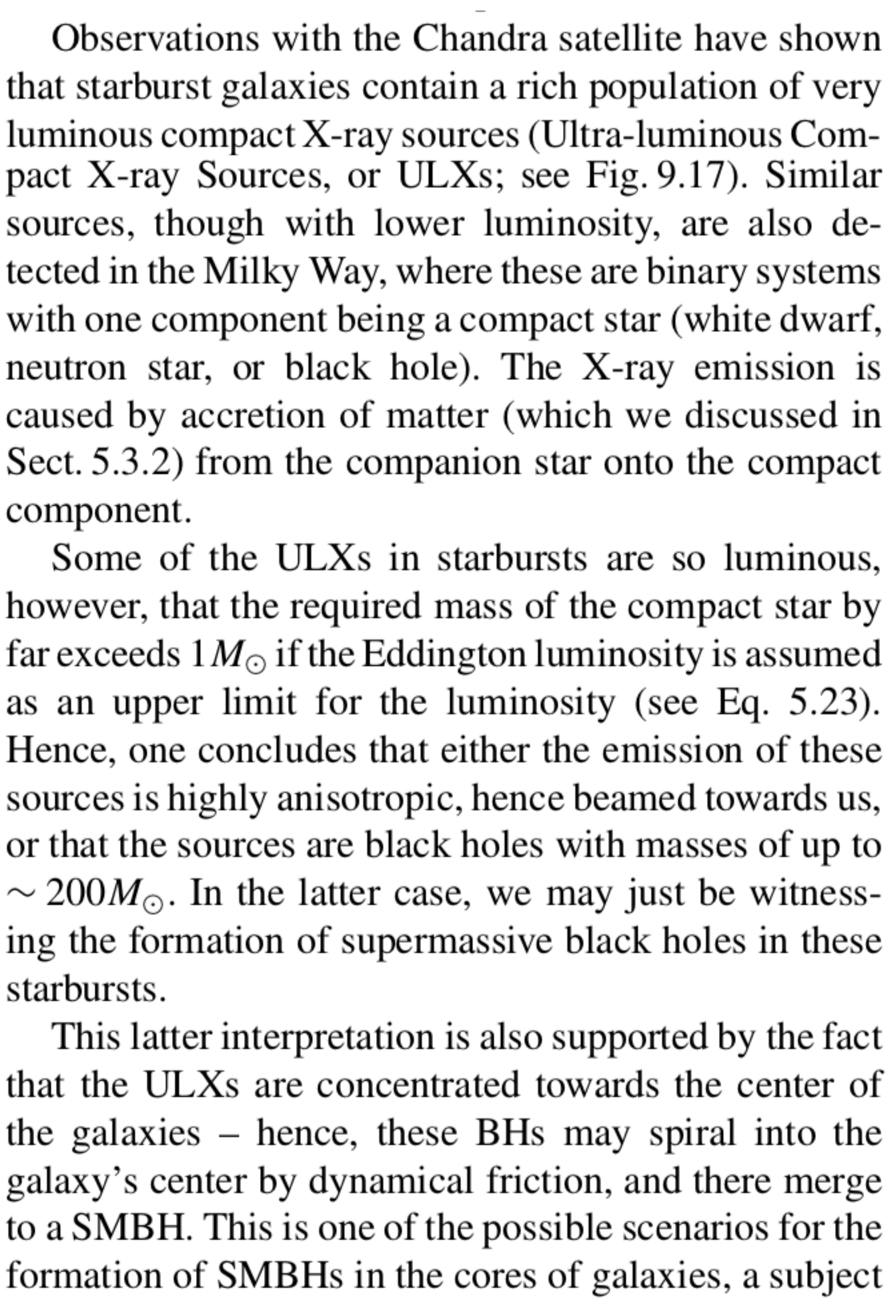

Observations with the Chandra satellite have shown that starburst galaxies contain a rich population of very luminous compact X-ray sources (Ultra-luminous Compact X-ray Sources, or ULXs; see Fig. 9.17). Similar sources, though with lower luminosity, are also detected in the Milky Way, where these are binary systems with one component being a compact star (white dwarf, neutron star, or black hole). The X-ray emission is caused by accretion of matter (which we discussed in Sect. 5.3.2) from the companion star onto the compact component.

Some of the ULXs in starbursts are so luminous, however, that the required mass of the compact star by far exceeds $1 M_\odot$ if the Eddington luminosity is assumed as an upper limit for the luminosity (see Eq. 5.23). Hence, one concludes that either the emission of these sources is highly anisotropic, hence beamed towards us, or that the sources are black holes with masses of up to $\sim 200 M_\odot$. In the latter case, we may just be witnessing the formation of supermassive black holes in these starbursts.

This latter interpretation is also supported by the fact that the ULXs are concentrated towards the center of the galaxies – hence, these BHs may spiral into the galaxy's center by dynamical friction, and there merge to a SMBH. This is one of the possible scenarios for the formation of SMBHs in the cores of galaxies, a subject

Discrete X-ray sources (ULXs)

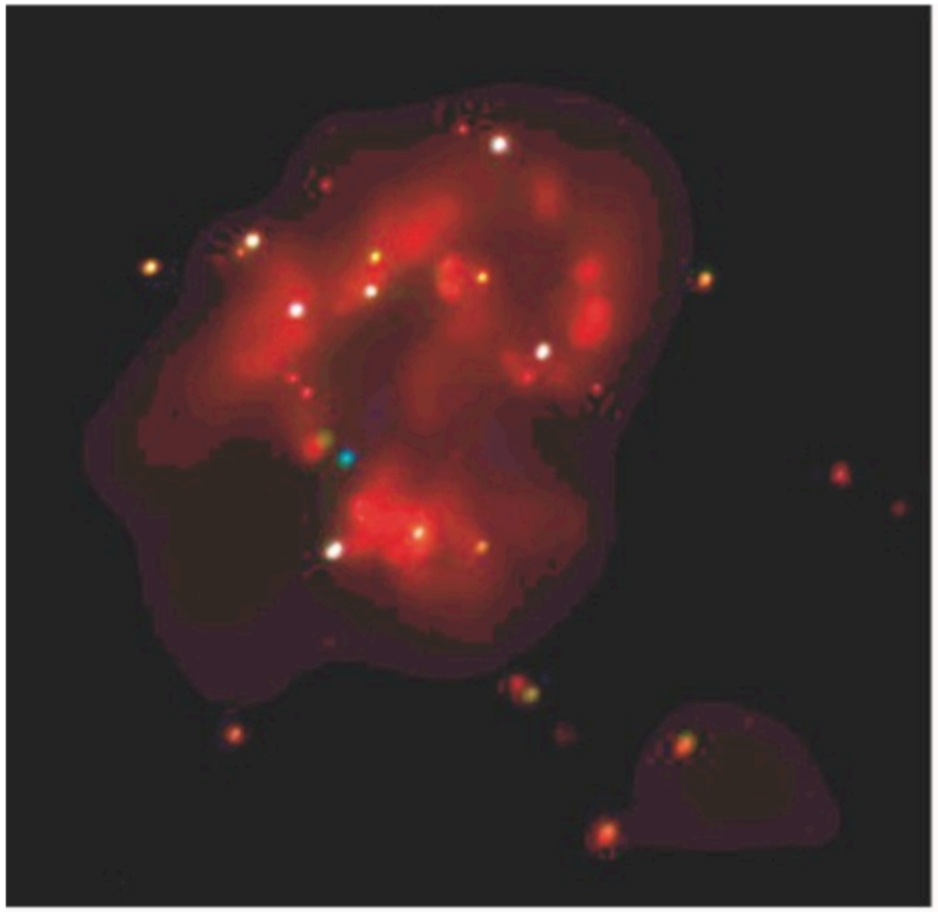

Fig. 9.17. Ultra-luminous Compact X-ray Sources (ULXs) in starburst galaxies. Upper left: the discrete X-ray sources in the Antenna galaxies; the size of the image is $4' \times 4'$.

Starburst Galaxies

ULXs in NGC 253

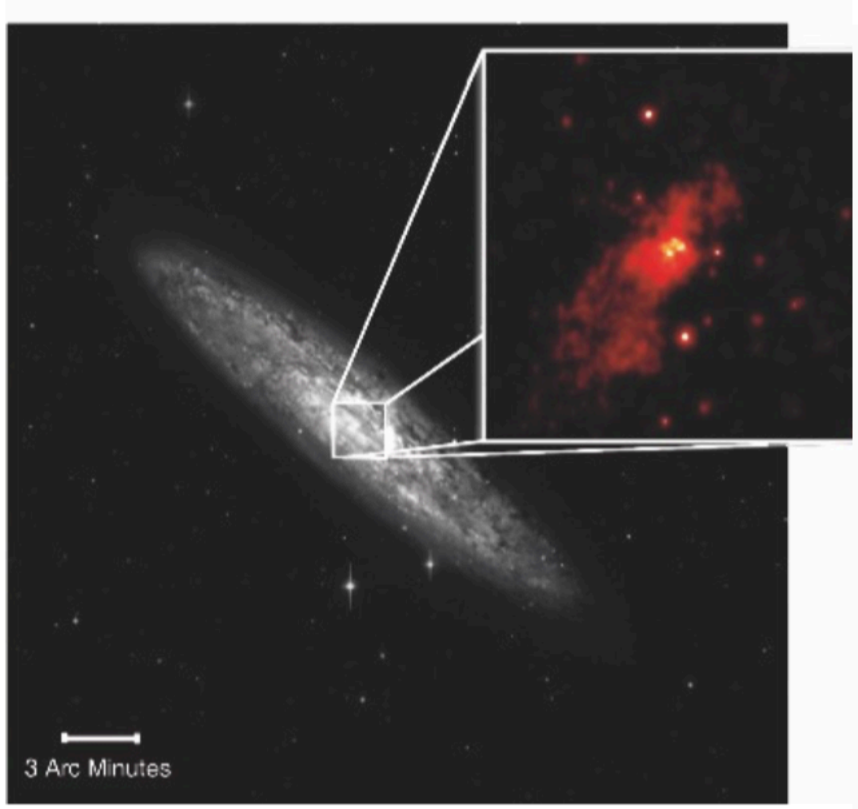

Fig. 9.17. Ultra-luminous Compact X-ray Sources (ULXs) ir starburst galaxies.

optical (image) and (inlaid) Chandra image of the starburst galaxy NGC 253. Four of the ULXs are located within one kiloparsec from the center of the galaxy. The X-ray image is 2!2 × 2!2.

ULXs in M82

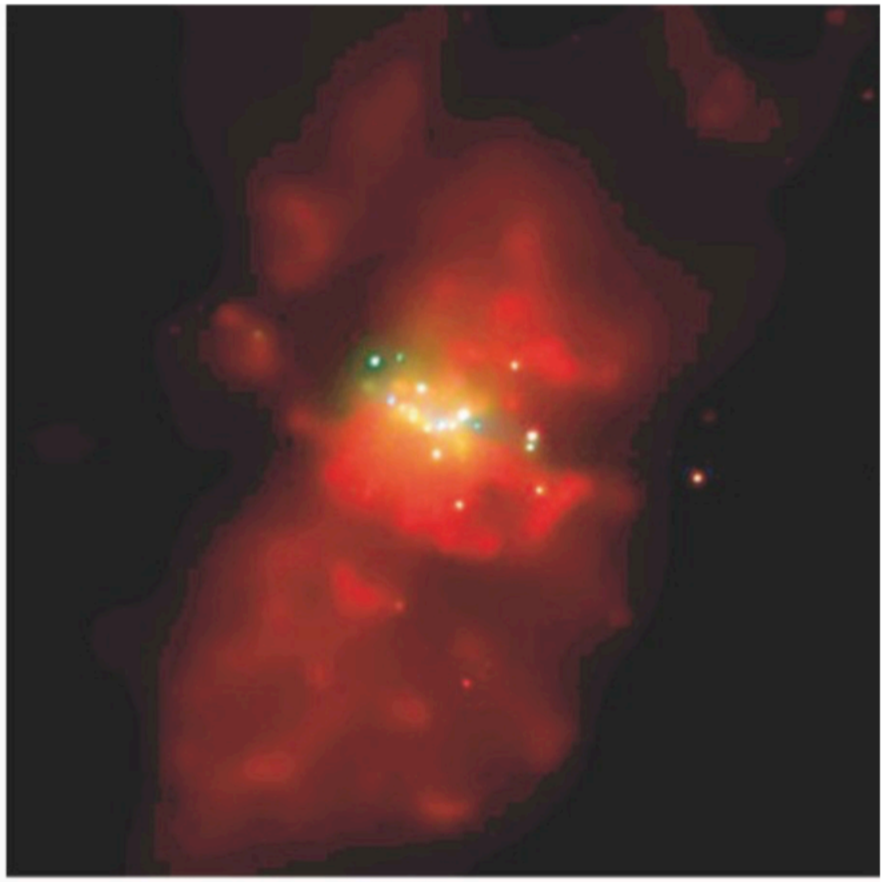

$5' \times 5'$ Chandra image of the starburst galaxy M82; the diffuse radiation (red) is emitted by gas at $T \sim 10^6$ K which is heated by the starburst and flows out from the central region of the galaxy. It is supposed that M82 had a collision with its companion M81 (see Fig. 6.7) within the last 10^8 yr, by which the starburst has been triggered.

Luminosity Function of ULXs

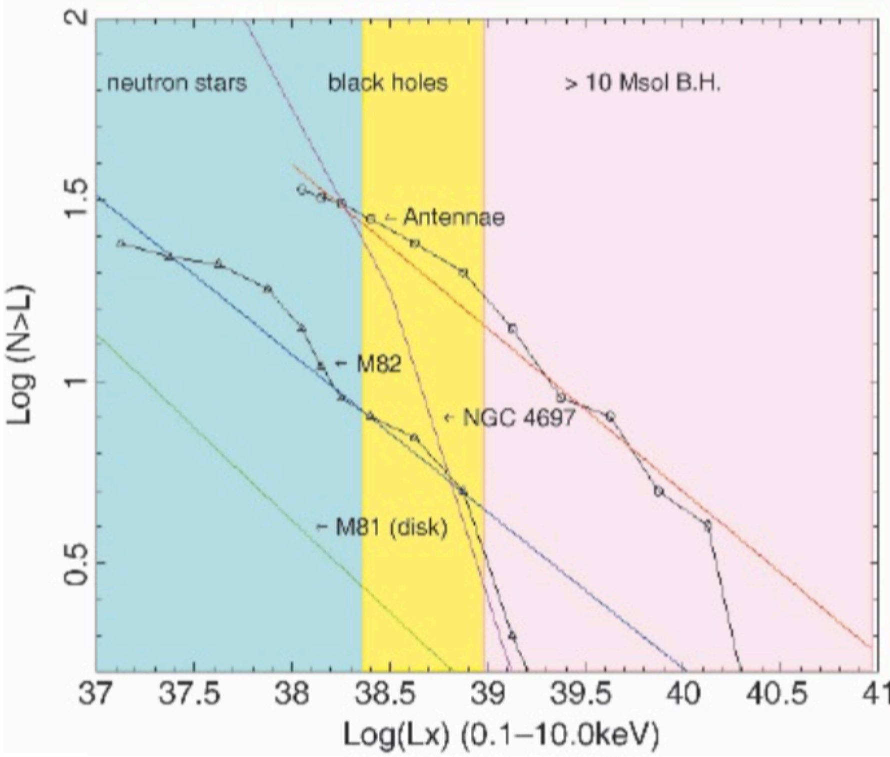

the luminosity function of the ULXs in some starburst galaxies

Extremely Red Objects (EROs)

As mentioned several times previously, the population of galaxies detected in a survey depends on the selection criteria. Thus, using the Lyman-break method, it is mainly those galaxies at high redshift which feature active star formation and therefore have a blue spectral distribution at wavelengths longwards of Lyα that are discovered. The development of NIR detectors enabled the search for galaxies at longer wavelengths. Of particular interest here are surveys of galaxies in the K-band, the longest wavelength window that is reasonably accessible from the ground (with the exception of the radio domain).

The NIR waveband is of particular interest because the luminosity of galaxies at these wavelengths is not dominated by young stars. As we have seen in Fig. 3.48, the luminosity in the K-band depends only weakly on the age of the stellar population, so that it provides a reliable measure of the total stellar mass of a galaxy.

In Fig. 9.18 the z-distribution of galaxies in the K20 survey is shown. In this survey, objects with $K_\mathrm{s} < 20$ have been selected in two fields with a combined area of 52 arcmin^2, where K$_\mathrm{s}$ is a filter at a wavelength slightly shorter than the classic K-band filter. After excluding stars and type 1 AGNs, 489 galaxies were found, 480 of which have had their redshifts determined. The median redshift in this survey is $z \approx 0.8$.

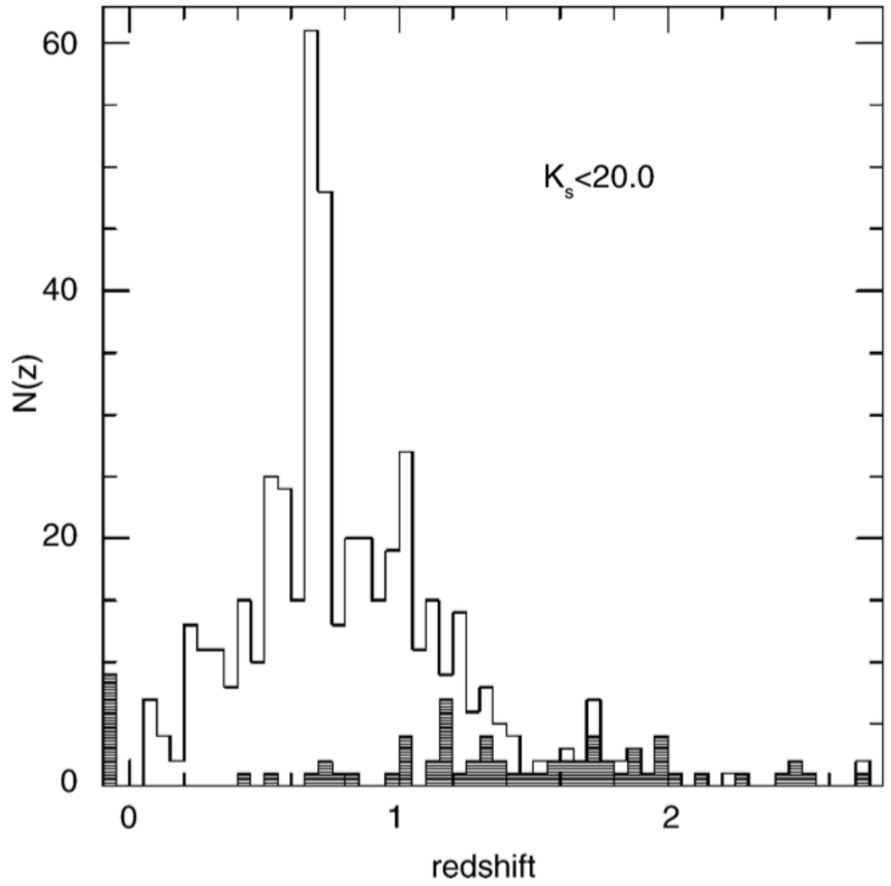

Fig. 9.18. Redshift distribution of galaxies with $K_\mathrm{s} < 20$, as measured in the K20 survey. The shaded histogram represents galaxies for which the redshift was determined solely by photometric methods. The bin at $z < 0$ contains those 9 galaxies for which it has not been possible to determine z. The peak at $z \sim 0.7$ is produced by two clusters of galaxies in the fields of the K20 survey

Extremely Red Objects (EROs)

Considering galaxies in a $(R-K)$ vs. K color–magnitude diagram (Fig. 9.19), one can identify a population of particularly red galaxies, thus those with a large $R-K$. These objects have been named *Extremely Red Objects* (*EROs*); about 10% of the galaxies in K-selected surveys at faint magnitudes are EROs, typically defined by $R-K>5$. Spectroscopic analysis of these galaxies poses a big challenge because an object with $K=20$ and $R-K>5$ necessarily has $R>25$, i.e., it is extremely faint in the optical domain of the spectrum. With the advent of 10-m class telescopes, spectroscopy of these objects has become possible in recent years.

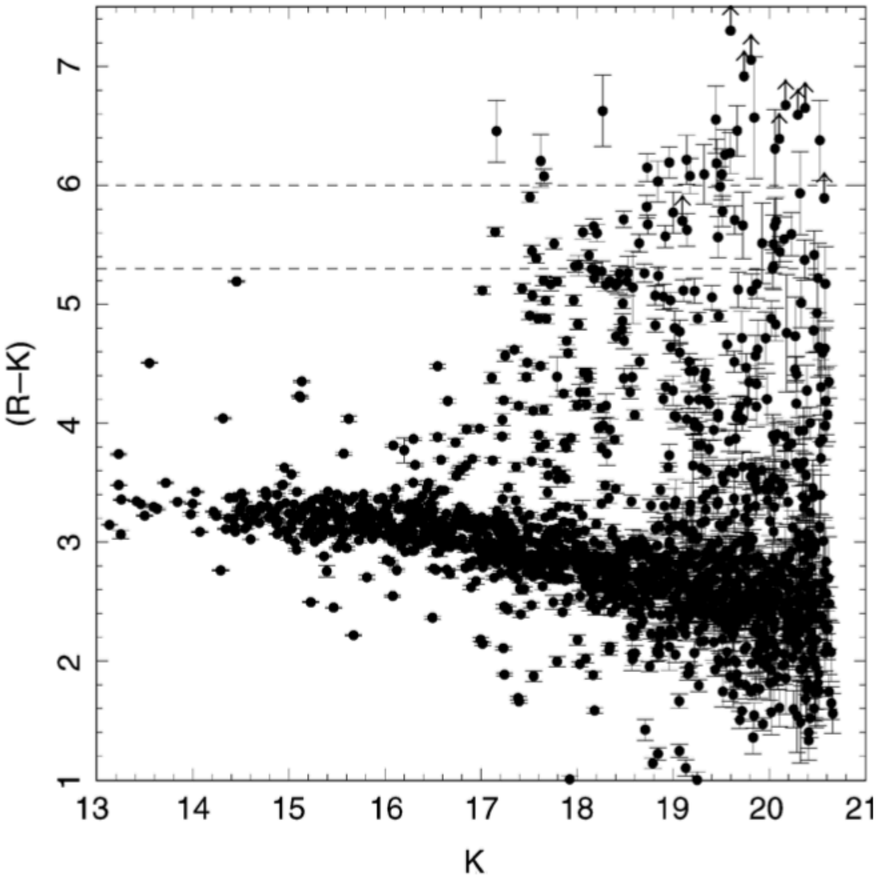

Fig. 9.19. Color–magnitude diagram, i.e., $R-K$ as a function of K, for sources in ten fields around clusters of galaxies. We see that for faint magnitudes (roughly $K \geq 19$), a population of sources with a very red color (about $R-K \geq 5.3$) turns up. These objects are called EROs

The Nature of EROs: Passive Ellipticals Versus Dusty Starbursts. From these spectroscopic results, it was found that the class of EROs contains rather different kinds of sources. To understand this point we will first consider the possible explanations for a galaxy with such a red spectral distribution. As a first option, the object may be an old elliptical galaxy with the 4000-Å break being redshifted to the red side of the R-band filter, i.e., typically an elliptical galaxy at $z \gtrsim 1.0$. For these galaxies to be sufficiently red to satisfy the selection criterion for EROs, they need to already contain an old stellar population by this redshift, which implies a very high redshift for the star formation in these objects; it is estimated from population synthesis models that their formation redshift must be $z_{\rm form} \gtrsim 2.5$. A second possible explanation for large $R-K$ is reddening by dust. Such EROs may be galaxies with active star formation where the optical light is strongly attenuated by dust extinction. If these galaxies are located at a redshift of $z \sim 1$, the measured R-band flux corresponds to a rest-frame emission in the UV region of the spectrum where extinction is very efficient.

Spectroscopic analysis reveals that both types of EROs are roughly equally abundant. Hence, about half of the EROs are elliptical galaxies that already have, at $z \sim 1$, a luminosity similar to that of today's ellipticals, and are at that epoch already dominated by an old stellar population. The other half are galaxies with active star formation which do not show a 4000-Å break but which feature the emission line of [OII] at $\lambda = 3727$ Å, a clear sign of star formation. Further analysis of EROs by means of very deep radio observations confirms the large fraction of galaxies with high star-formation rates. Utilizing the close relation of radio emissivity and FIR luminosity, we find a considerable fraction of EROs to be ULIRGs at $z \sim 1$.

Sub millimiter sources

FIR emission from hot dust is one of the best indicators of star formation. However, observations in this waveband are only possible from space, such as was done with the IRAS and ISO satellites. Dust emission has its maximum at about 100 µm, which is not observable from the ground. At longer wavelengths there are spectral windows where observations through the Earth's atmosphere are possible, for instance at 450 µm and 850 µm in the submillimeter waveband. However, the observing conditions at these wavelengths are extremely dependent on the amount of water vapor in the atmosphere, so that the observing sites must by dry and at high elevations. In the submillimeter (sub-mm) range, the long wavelength domain of thermal dust radiation can be observed, which is illustrated in Fig. 9.20.

Since about 1998 sub-mm astronomy has experienced an enormous boom, with two instruments having been put into operation: the Submillimeter Common User Bolometer Array (SCUBA), operating at 450 µm and 850 µm, with a field-of-view of 5 arcmin^2, and the Max-Planck Millimeter Bolometer (MAMBO), operating at 1300 µm. Both are bolometer arrays which initially had 37 bolometers each, but which since then have been upgraded to a considerably larger number of bolometers. Figure 9.21 shows a $20' \times 17'$ MAMBO image of a field in the region of the COSMOS survey.

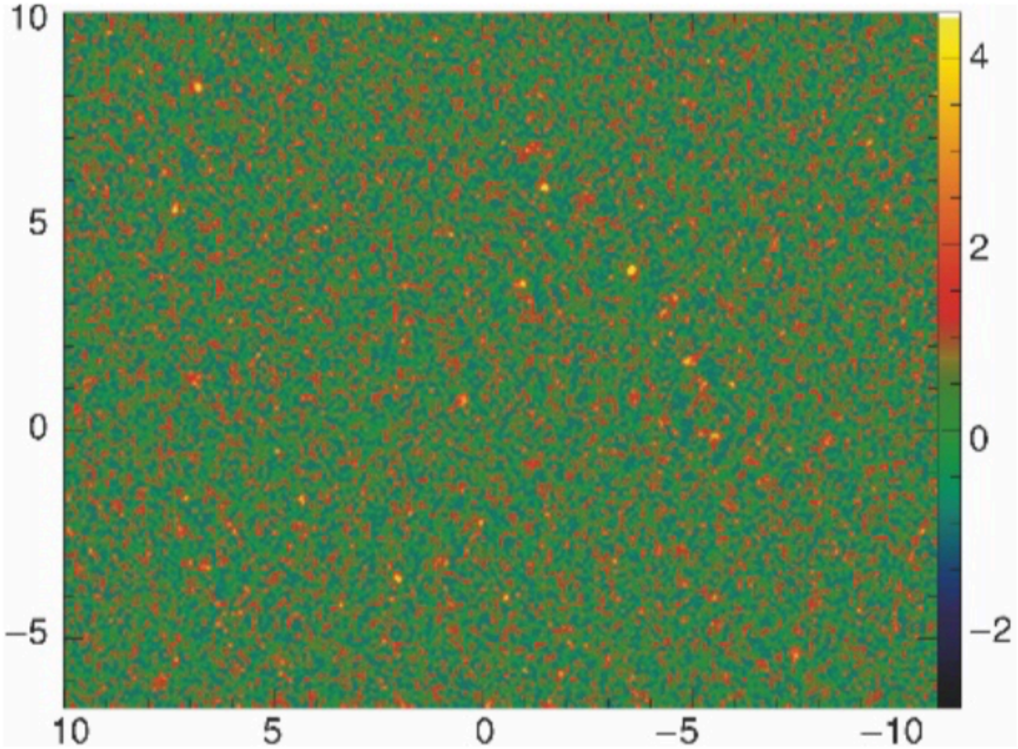

Fig. 9.21. The image shows a field of $20' \times 17'$ in the region of the COSMOS survey, observed by the 117-channel MAMBO instrument at the IRAM 30-m telescope on Pico Veleta. Coded in color is the signal-to-noise ratio of the map, where the noise level is about 0.9 mJy per $11''$ beam. About a dozen sources with $S/N \geq 4$ are visible

Sub millimiter sources

The Negative K-Correction of Submillimeter Sources. The emission of dust at these wavelenghs is described by a Rayleigh–Jeans spectrum, modified by an emissivity function that depends on the dust properties (chemical composition, distribution of dust grain sizes); typically, one finds

$$S_\nu \propto \nu^{2+\beta} \quad \text{with} \quad \beta \sim 1 \ldots 2 \, .$$

This steep spectrum for frequencies below the peak of the thermal dust emission at $\lambda \sim 100\,\mu\mathrm{m}$ implies a very strong negative K-correction (see Sect. 5.6.1) for wavelengths in the sub-mm domain: at a fixed observed wavelength, the rest-frame wavelength becomes increasingly smaller for sources at higher redshift, and there the emissivity is larger. As Fig. 9.22 demonstrates, this spectral behavior causes the effect that the flux in the sub-mm range does not necessarily decrease with redshift. For $z \lesssim 1$, the $1/D^2$-dependence of the flux dominates, so that up to $z \sim 1$ sources at fixed luminosity get fainter with increasing z. However, between $z \sim 1$ and $z \sim z_{\rm flat}$ the sub-mm flux as a function of redshift remains nearly constant or even increases with z, where $z_{\rm flat}$ depends on the dust temperature $T_{\rm d}$; for $T_{\rm d} \sim 40$ K and $\lambda \sim 850\,\mu\mathrm{m}$ one finds $z_{\rm flat} \sim 8$. We therefore have the quite amazing situation that sources appear brighter when they are moved to larger distances. This is caused by the very negative K-correction which more than compensates for the $1/D^2$-decrease of the flux. Only for $z > z_{\rm flat}$ does the flux begin to rapidly decrease with redshift, since then, due to redshift, the corresponding rest-frame frequency is shifted to the far side of the maximum of the dust spectrum (see Fig. 9.20). Hence, a sample of galaxies that is flux-limited in the sub-mm domain should have a very broad z-distribution. The dust temperature is about $T_{\rm d} \sim 20$ K for low-redshift spirals, and $T_{\rm d} \sim 40$ K is a typical value for galaxies at higher redshift featuring active star formation. The higher $T_{\rm d}$, the smaller the sub-mm flux at fixed bolometric luminosity.

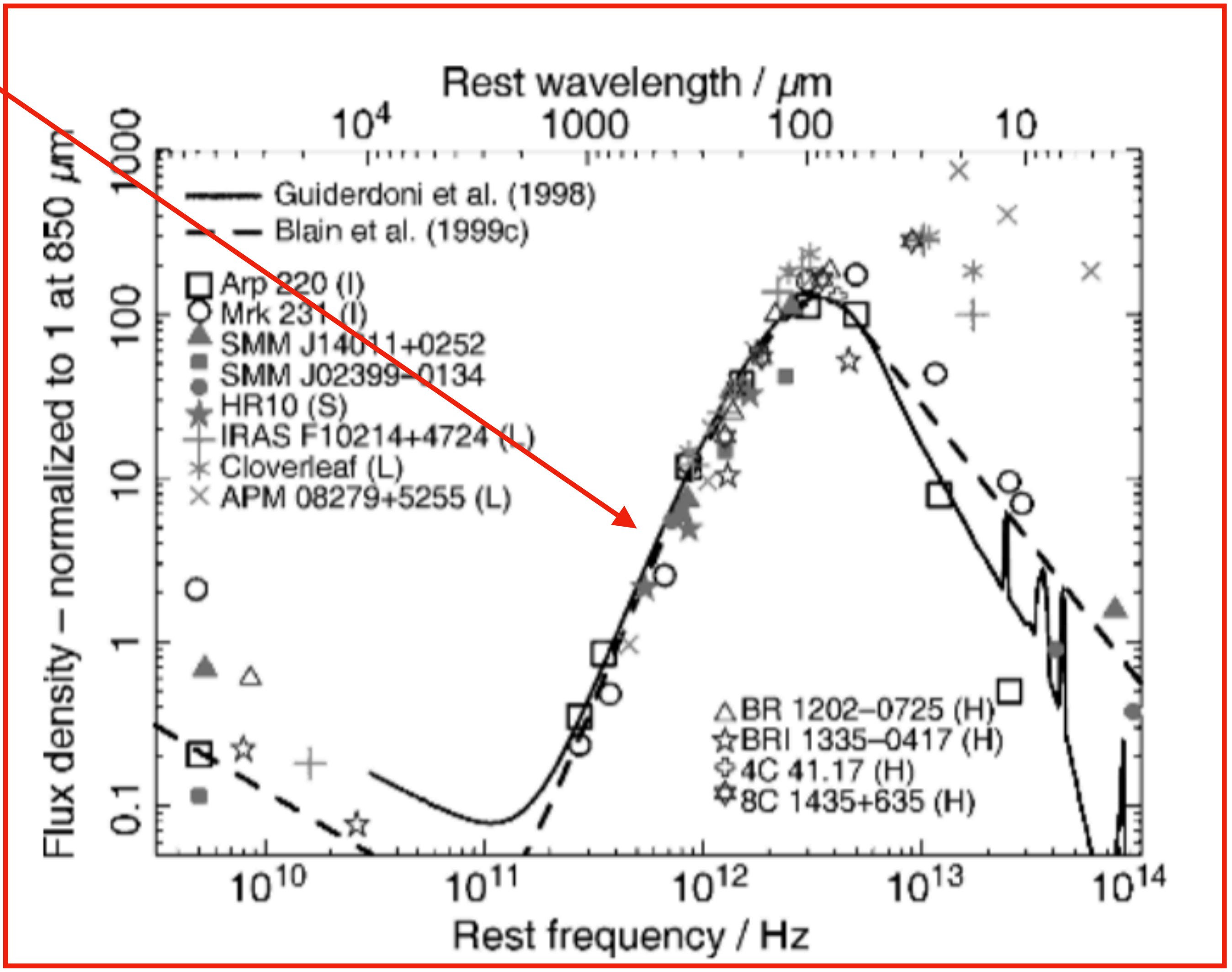

Fig. 9.20. Spectral energy distribution of some dusty galaxies with known redshift z (symbols), together with two model spectra (curves). Four types of galaxy are distinguished: (I) IRAS galaxies at low z; (S) luminous sub-mm galaxies; (L) distant sources that are magnified by the gravitational lens effect and multiply imaged; (H) AGNs. Only a few sources among the lens systems (presumably due to differential magnification) and the AGNs deviate significantly from the model spectra

Sub millimiter sources

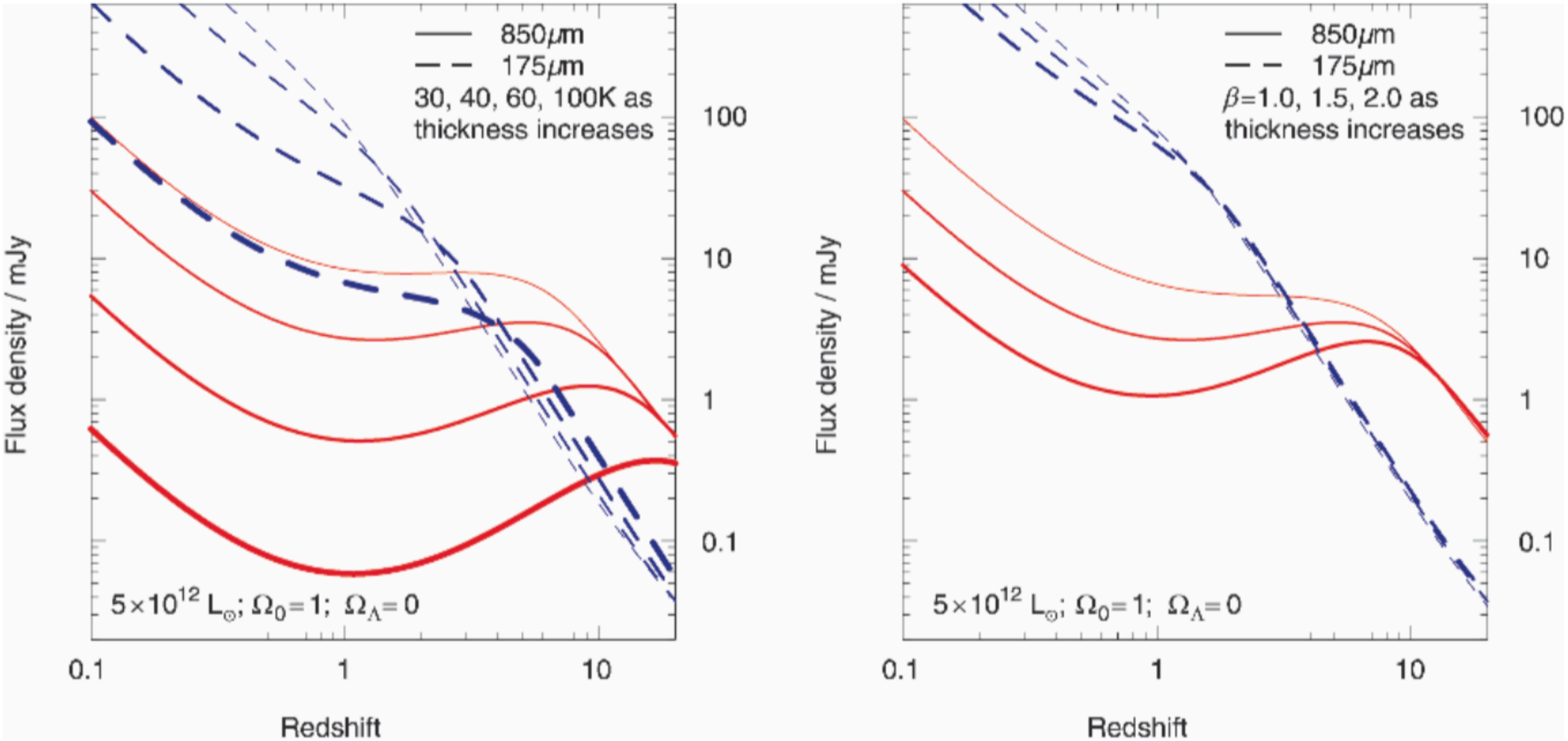

Fig. 9.22. Predicted flux from dusty galaxies as a function of redshift. The bolometric luminosity of these galaxies is kept constant. The solid red and the blue dashed curves show the flux at $\lambda = 850$ μm and $\lambda = 175$ μm, respectively. On the right, the index β of the dust emissivity is varied, and the temperature of the dust $T_d = 38$ K is kept fixed. On the left, $\beta = 1.5$ is fixed and the temperature is varied. It is remarkable how flat these curves are over a very wide range in redshift, in particular at 850 μm; this is due to the very strong negative K-correction which derives from the spectral behavior of thermal dust emission, shown in Fig. 9.20

Sub millimiter sources

Optical counterparts

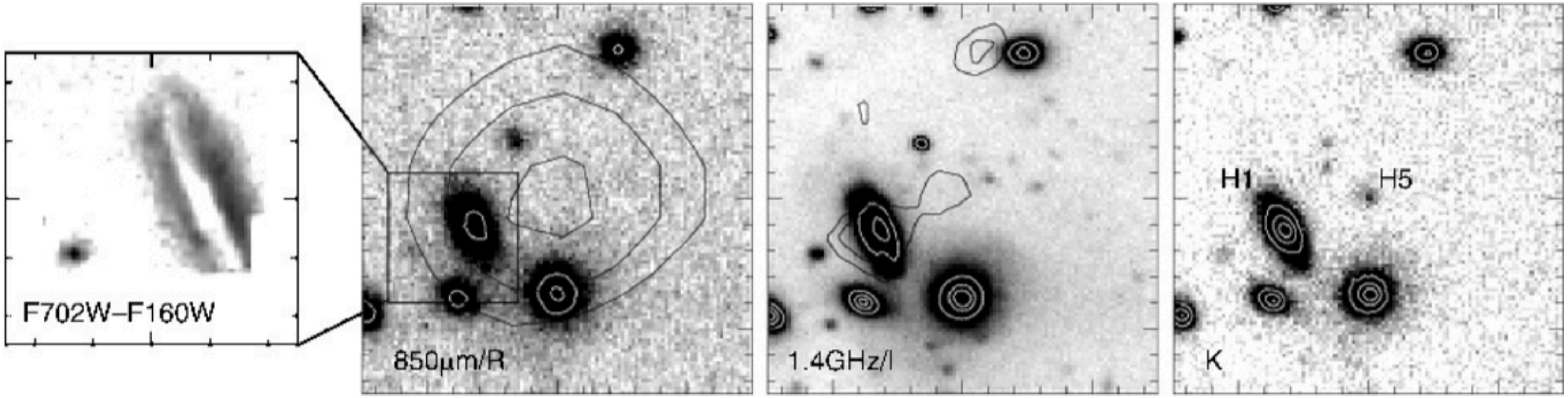

Fig. 9.23. The sub-mm galaxy SMM J09429+4658. The three images on the right have a side length of 30″ each, centered on the center of the error box of the 850 μm observation. The smaller image on left is the difference of two HST images in red and infrared filters, showing the dust disk in the spiral galaxy H1. The second image from the left displays an R-band image, superposed with the contours of the SCUBA 850 μm emission. The second image from the right is an I-band image, superposed with the contours of radio emission at 1.4 GHz, and the right-most panel shows a K-band image. The radio contours show emission from the galaxy H1 ($z = 0.33$), but also weaker emission right at the center of the sub-mm map. In the K-band, a NIR source (H5) is found exactly at this position. It remains unclear which of these two sources is the sub-mm source, but the ratio of sub-mm to 1.4-GHz emission would be atypical if H1 is identified with the sub-mm source

Cosmic Background at various wavelengths

Fig. 9.24. Spectrum of cosmic background radiation, plotted as νI_ν versus wavelength. Besides the CMB, background radiation exists in the radio domain (cosmic radio background, CRB), in the infrared (CIB), in the optical/UV (CUVOB), in the X-ray (CXB), and at gamma-ray energies (CGB). With the exception of the CMB, probably all of these backgrounds can be understood as a superposition of the emission from discrete sources. Furthermore, this figure shows that the energy density in the CMB exceeds that of other radiation components, as was assumed when we considered the radiation density in the Universe in Chap. 4

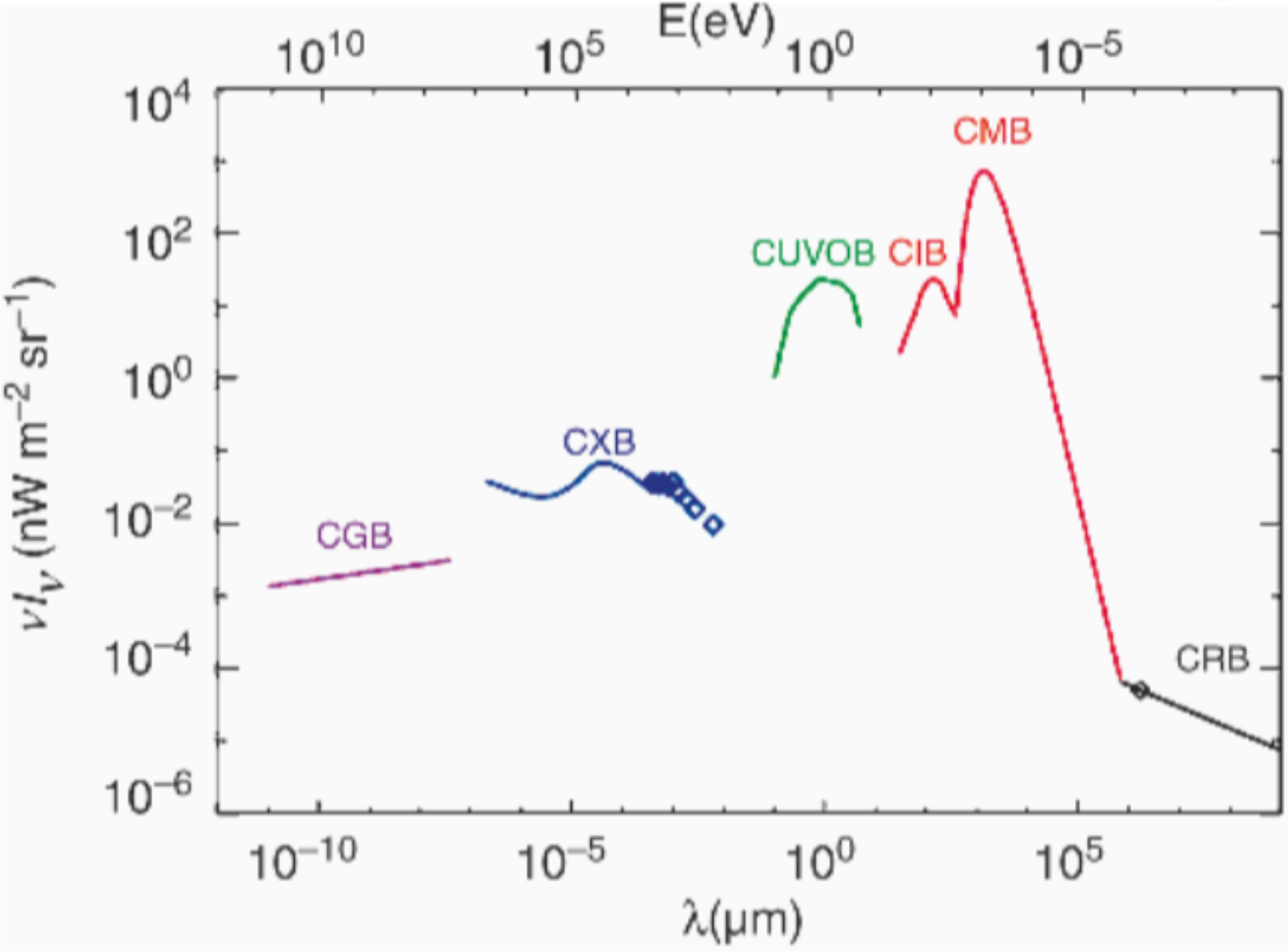

Discrete sources of the CXB

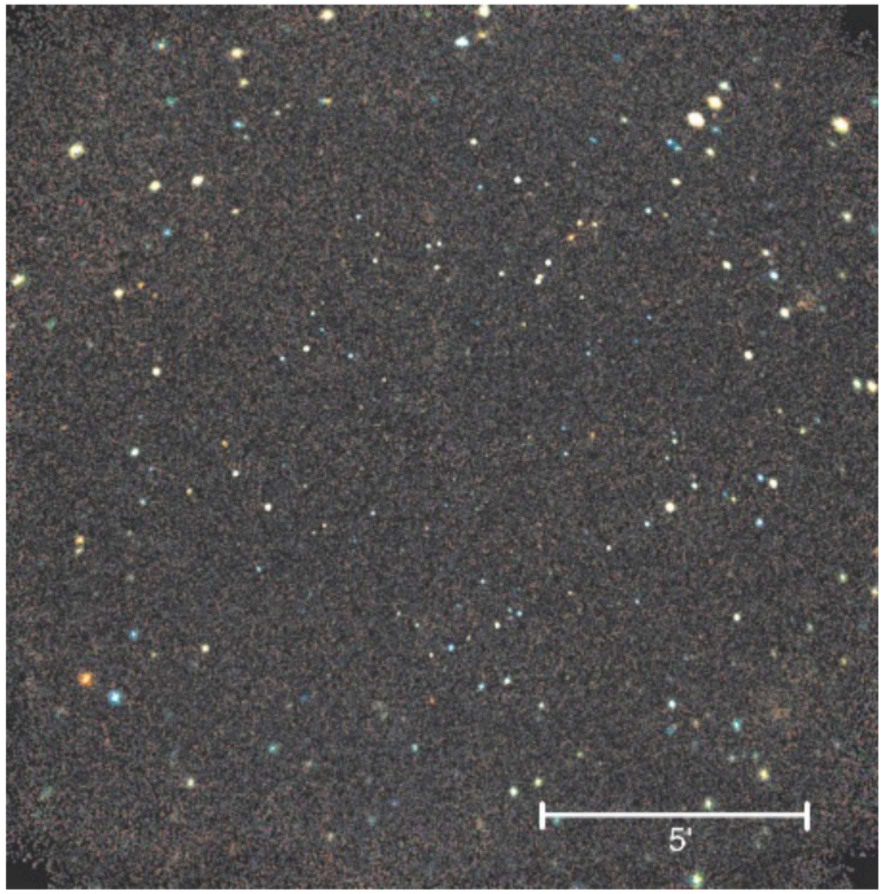

Fig. 9.27. The Chandra Deep Field South, a deep X-ray image of a 16′ × 16′ field with an exposure time of 10^6 s – one of the deepest X-ray images ever obtained. Most of the sources visible in this field are AGNs, but galaxies, groups, and clusters are also detected. The photon energy is color-coded, from lower to higher energies in red, yellow, and blue. One of the sources in this field is a very distant QSO of Type 2. A radial variation of the PSF in the field is visible by the increasing size of individual sources towards the edges

Reionization of the universe

After recombination at $z \sim 1100$, the intergalactic gas became neutral, with a residual ionization of only $\sim 10^{-4}$. Had the Universe remained neutral we would not be able to receive any photons that were emitted bluewards of the Lyα line of a source, because the absorption cross-section for Lyα photons is too large (see Eq. 8.16). Since such photons are observed from QSOs, as can be seen for instance in the spectra of the $z > 5.7$ QSOs in Fig. 9.28, and since an appreciable fraction of homogeneously distributed neutral gas in the intergalactic medium can be excluded for $z \lesssim 5$, from the tight upper bounds on the strength of the Gunn–Peterson effect (Sect. 8.5.1) the Universe must have been reionized between the recombination epoch and the redshift $z \sim 6.5$ of the most distant known sources. From the WMAP results (see Sect. 8.7.1) one concludes that reionization must have taken place at very high redshift, $z \sim 15$.

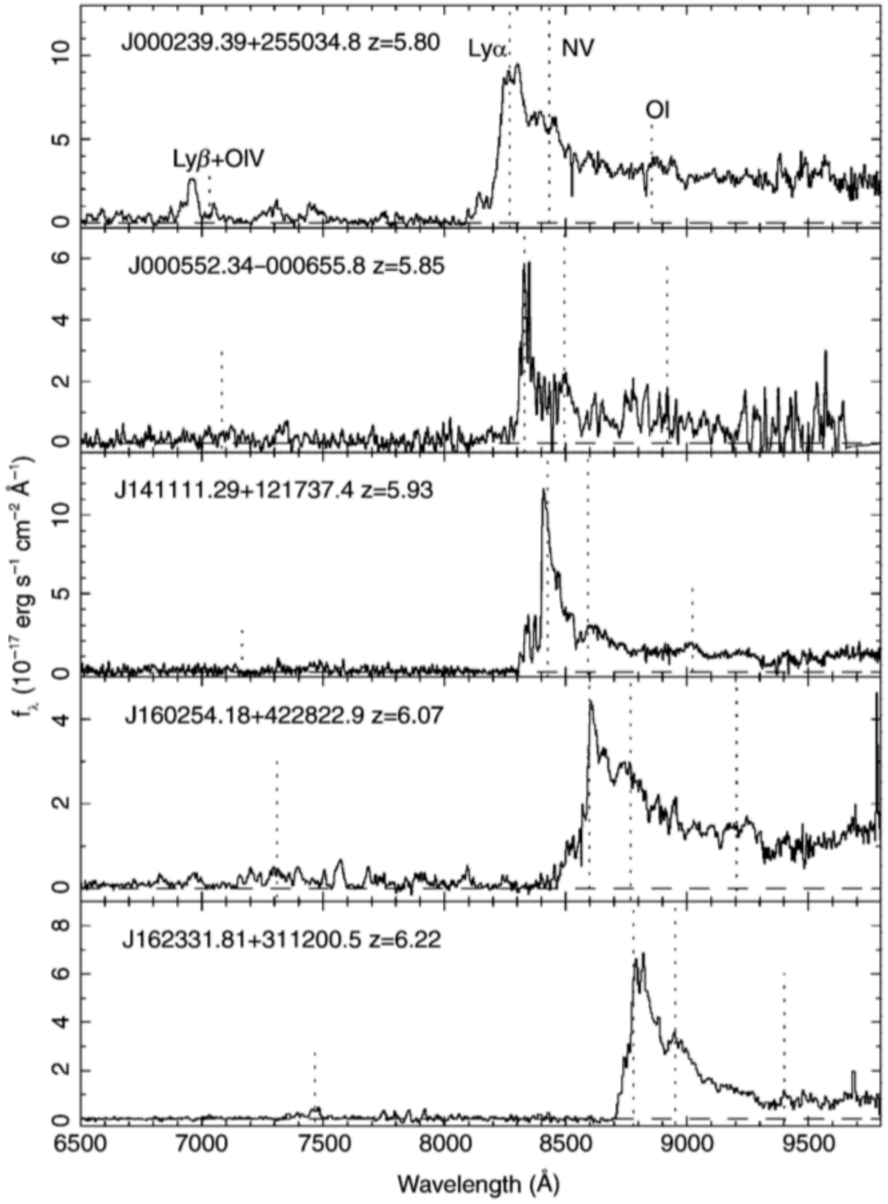

Fig. 9.28. Spectra of five QSOs at redshifts $z > 5.7$, discovered in multicolor data from the Sloan Digital Sky Survey. The positions of the most important emission lines are marked. Particularly remarkable is the complete lack of flux bluewards of the Lyα emission line in some of the QSOs, indicating a strong Gunn–Peterson effect. However, this absorption is not complete in all QSOs, which points at strong variations in the density of neutral hydrogen in the intergalactic medium at these high redshifts. Either the hydrogen density varies strongly for different lines-of-sight, or the degree of ionization is very inhomogeneous

Reionization of the universe

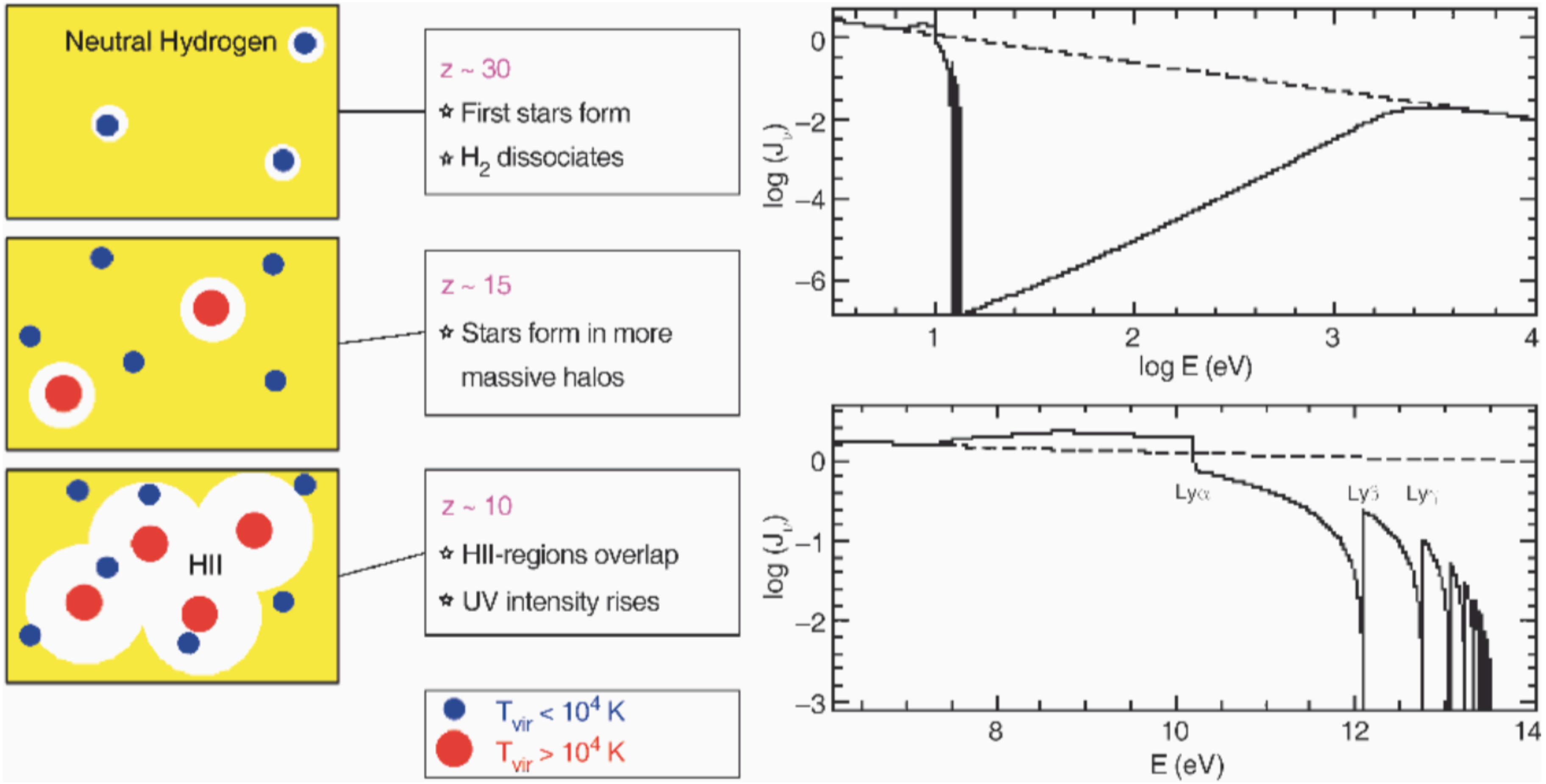

Fig. 9.30. Left: a sketch of the geometry of reionization is shown: initially, relatively low-mass halos collapse, a first generation of stars ionizes and heats the gas in these halos. By heating, the temperature increases so strongly (to about $T \sim 10^4$ K) that gas can escape from the potential wells; these halos may never again form stars efficiently. Only when more massive halos have collapsed will continuous star formation set in. Ionizing photons from this first generation of hot stars produce HII regions around their halos, which is the onset of reionization. The regions in which hydrogen is ionized will grow until they start to overlap; at that time, the flux of ionizing photons will strongly increase. Right: the average spectrum of photons at the beginning of the reionization epoch is shown; here, it has been assumed that the flux from the radiation source follows a power law (dashed curve). Photons with an energy higher than that of the Lyα transition are strongly suppressed because they are efficiently absorbed. The spectrum near the Lyman limit shows features which are produced by the combination of breaks corresponding to the various Lyman lines, and the redshifting of the photons

Reionization of the universe

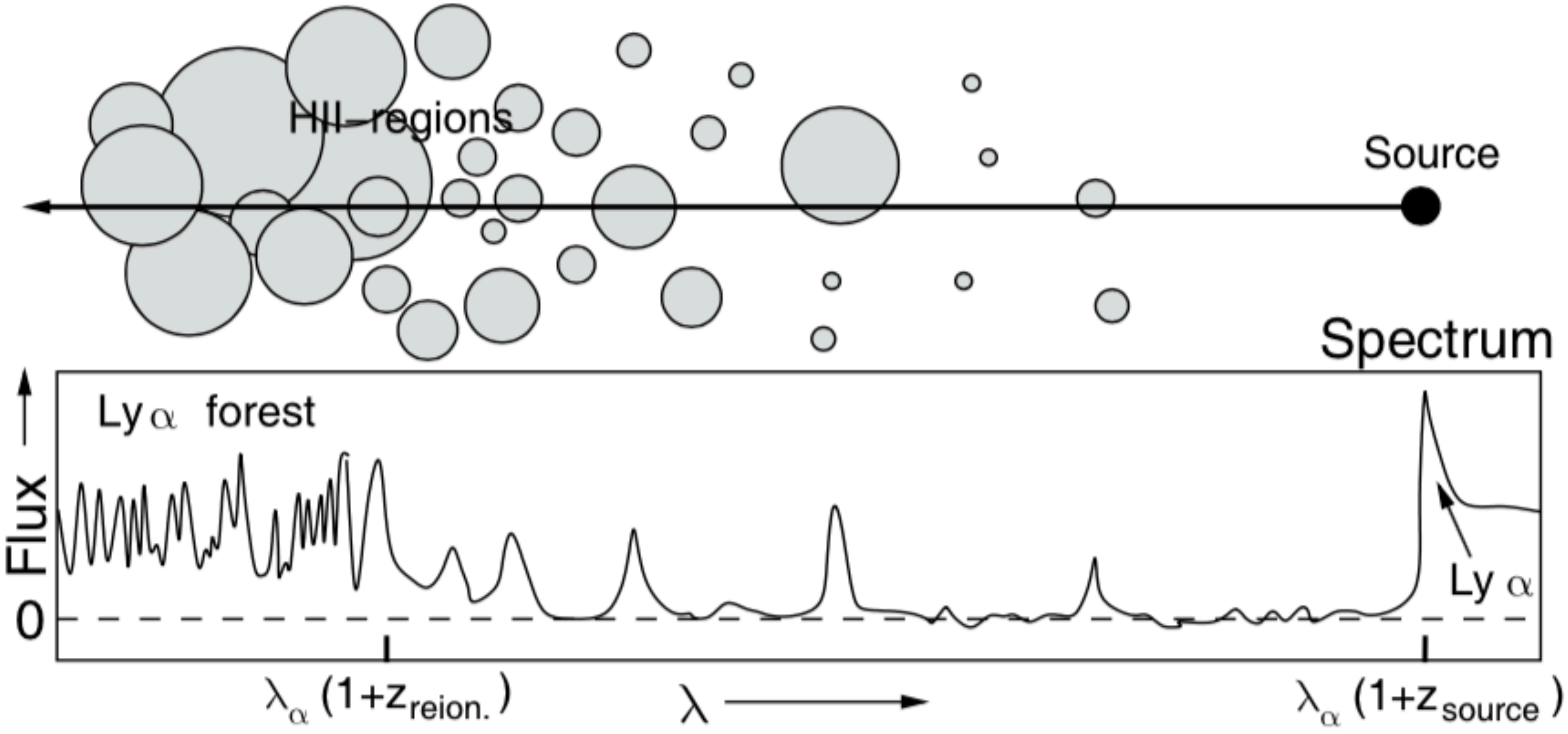

Fig. 9.31. Sketch of a potential observation of reionization: light from a very distant QSO propagates through a partially ionized Universe; at locations where it passes through HII regions, radiation will get through – flux will be visible at the corresponding wavelengths. When the HII regions start to overlap, the normal Lyα forest will be produced

Main Sequence of Star Forming Galaxies

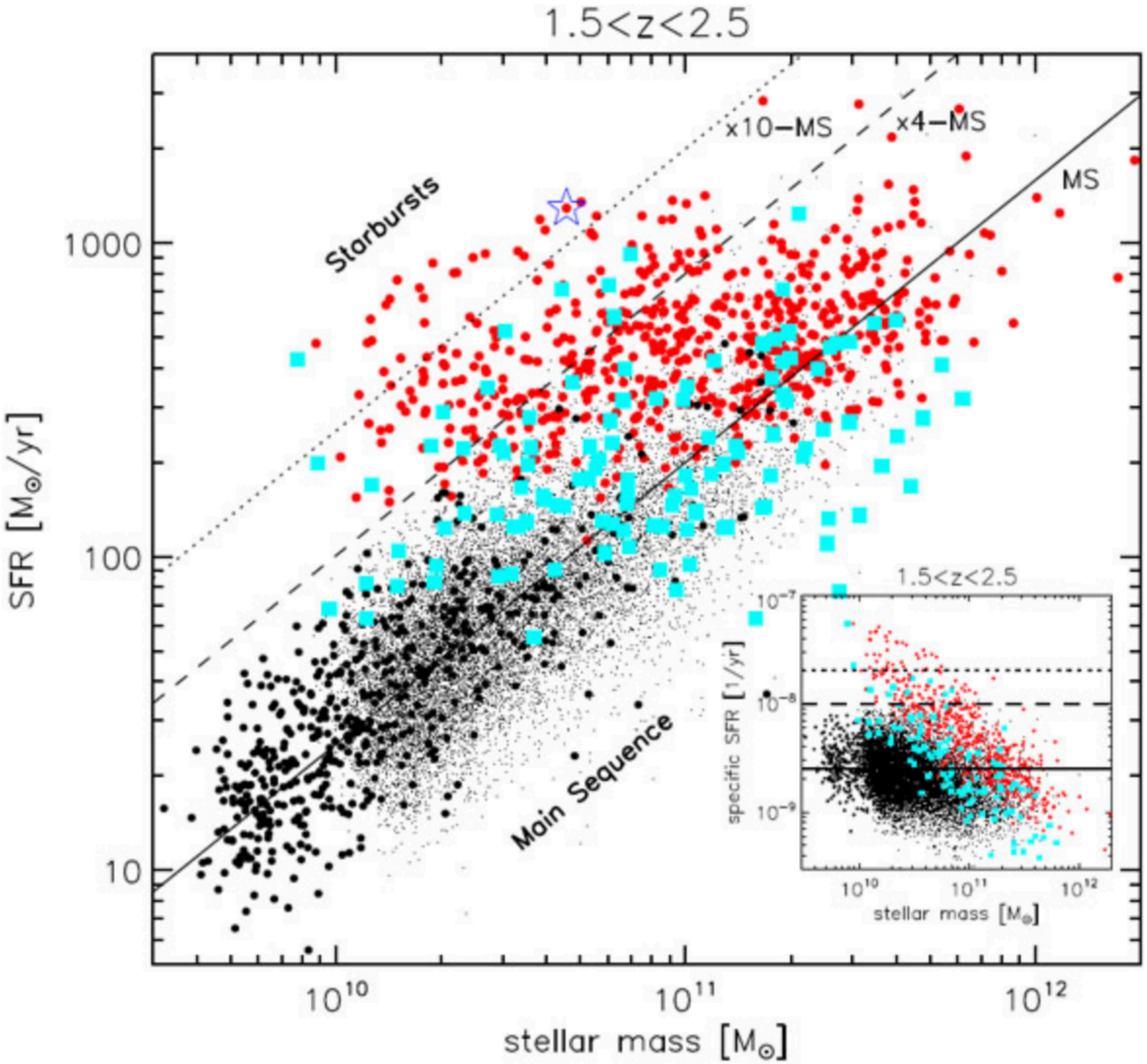

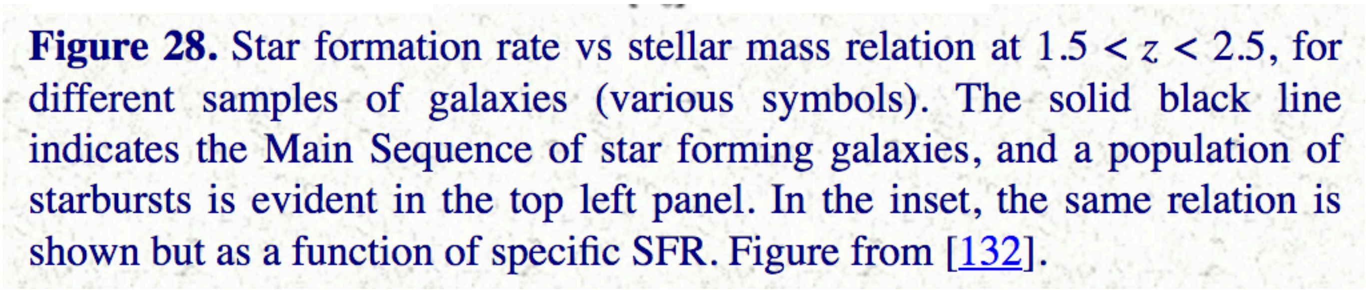

Figure 28. Star formation rate vs stellar mass relation at $1.5 < z < 2.5$, for different samples of galaxies (various symbols). The solid black line indicates the Main Sequence of star forming galaxies, and a population of starbursts is evident in the top left panel. In the inset, the same relation is shown but as a function of specific SFR. Figure from [132].

Main Sequence of Star Forming Galaxies

Santini et al.

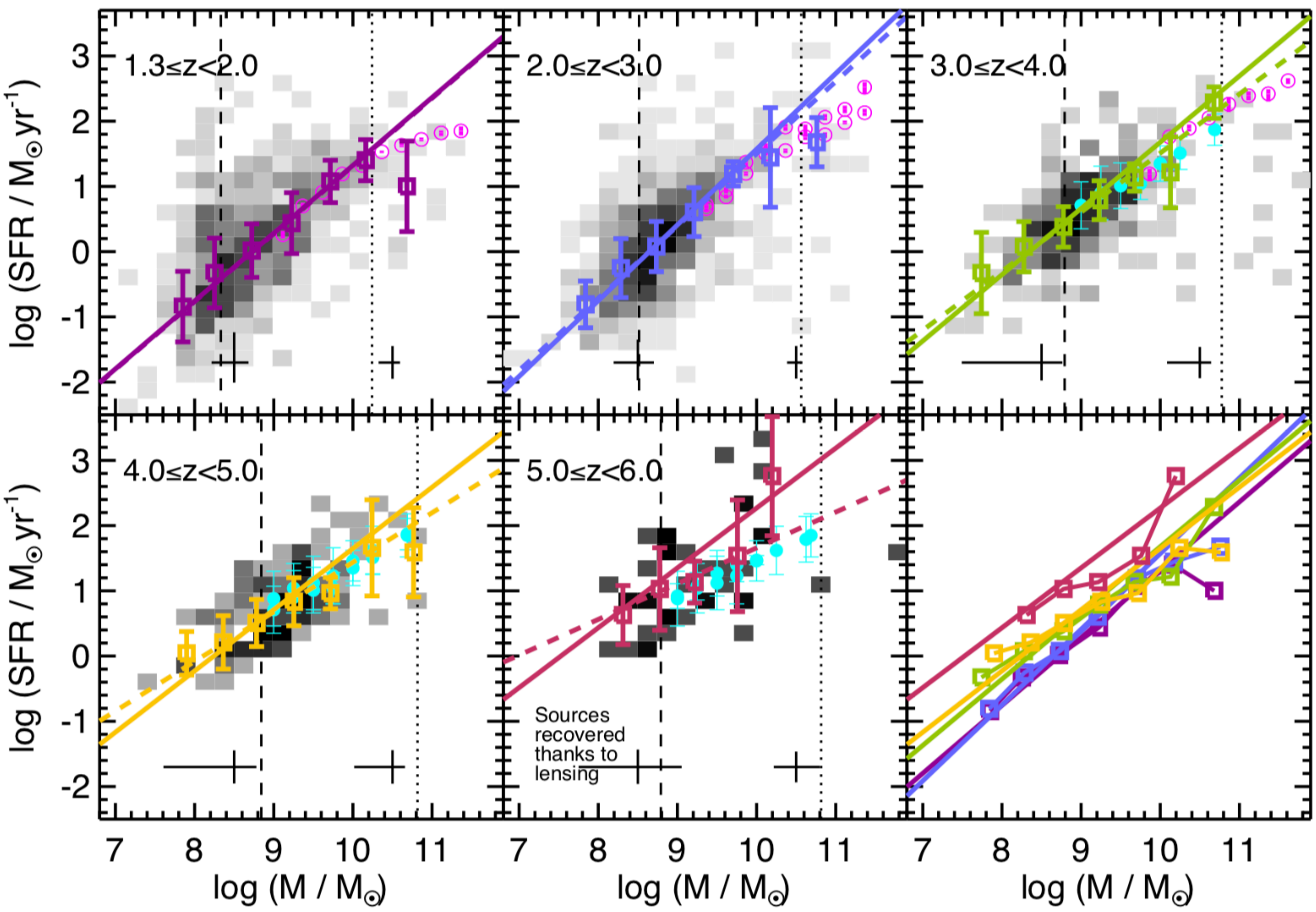

Figure 2. Relation between the SFR and the stellar mass in different redshift bins. The plane is coloured according to the density of sources, increasing from lightest (0.1% of the total number of sources in that redshift interval) to darkest (6.3%) shades on a linear scale. The open boxes show 2σ clipped average values. The dashed coloured lines show the best-fit linear relation obtained with a 2σ clipping procedure at stellar masses below the redshift-dependent turnover mass fitted by Tomczak et al. (2016), to avoid the region where the linearity breaks up. The solid coloured lines show the "true" underlying Main Sequence, after correcting for the Eddington bias. At the bottom of each redshift panel, the error bars show the median 1σ uncertainties on stellar masses and SFRs for galaxies in the $\log M/M_\odot$=8-9 and 10-11 bins. The dashed vertical lines show the observational mass completeness limit of the sample at the central redshift in each bin: all sources to the left of these lines have been recovered thanks to gravitational lensing. The dotted vertical lines show the turnover mass at the central redshift in each bin as taken from Tomczak et al. (2016). At $z > 4$ we adopted the threshold observed at $z = 4$. The open magenta and solid cyan circles show the results of Tomczak et al. (2016) and Salmon et al. (2015), respectively. *Bottom right panel:* Average values and "true" Main Sequence relations in all redshift bins, colour-coded accordingly.

Main Sequence of Star Forming Galaxies

A&A 533, A119 (2011)

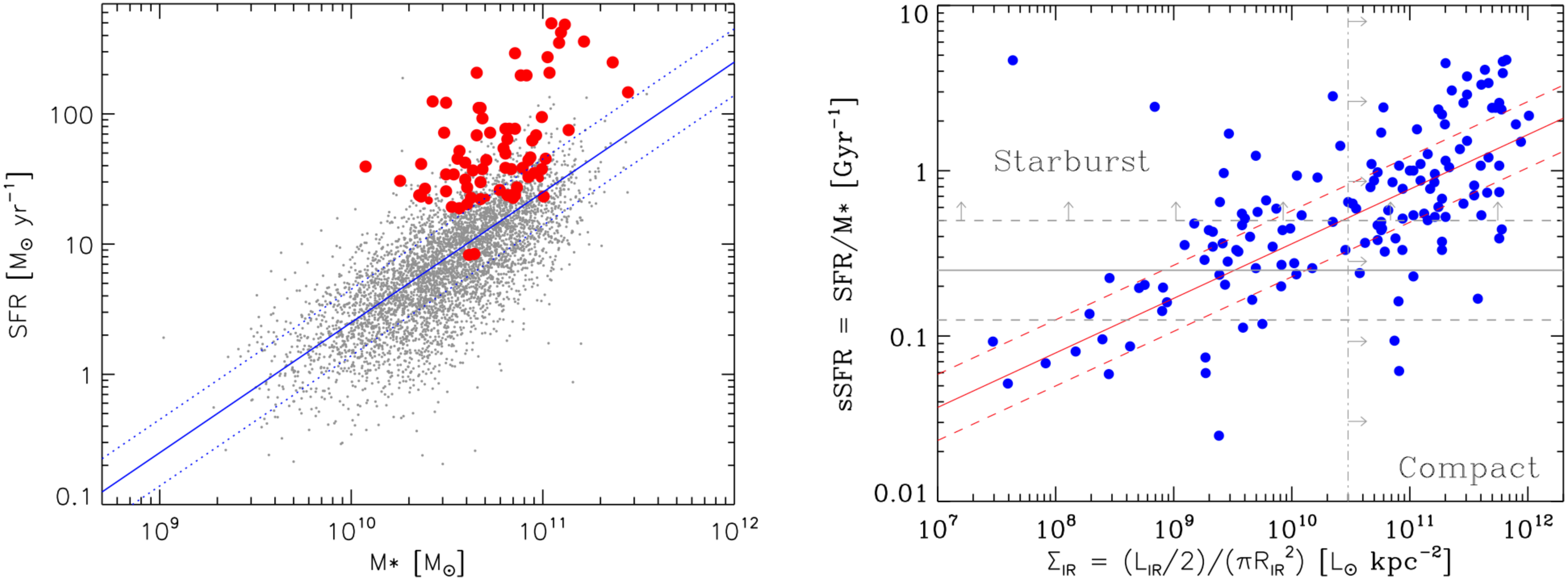

Fig. 16. *Left*: SFR – M_* correlation at $z \sim 0$. Galaxies classified as compact are marked with large filled red dots. Solid line: fit to the main sequence SFR–M_* relation: $SFR \propto M_\star/[4\times10^9\ M_\odot]$. Dotted lines: 16th and 84th percentiles of the distribution around the sliding median (0.26 dex). *Right*: relation of the sSFR and IR surface brightness of galaxies for which a radio size was estimated. The vertical dashed line illustrates the threshold above which galaxies have been classified as compact. The solid and dashed red lines are a fit to the sliding median of the relation (Eq. (11)) and its 68% dispersion.

Main Sequence of Star Forming Galaxies

D. Elbaz et al.: GOODS–*Herschel*: an infrared main sequence for star-forming galaxies

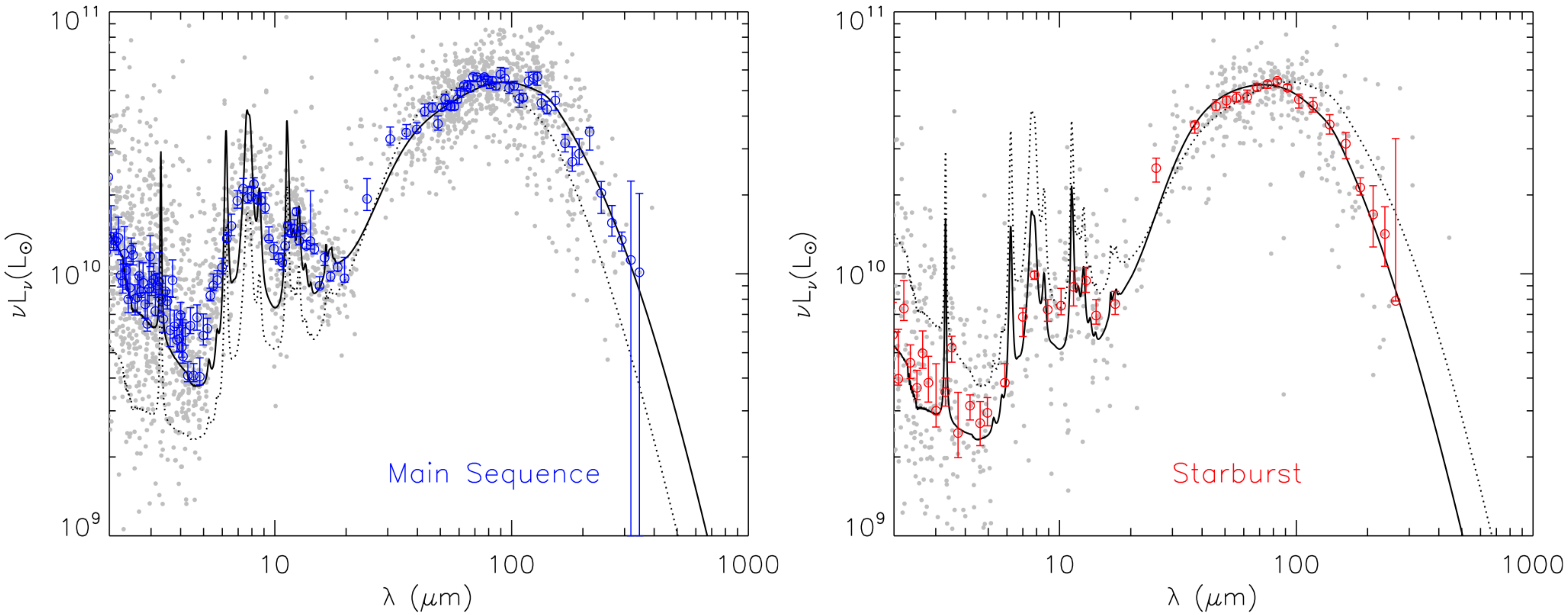

Fig. 21. Composite spectral energy distribution of the typical main sequence galaxy (*left*; IR8 = 4 ± 2, see Eq. (5)) and starburst (*right*; IR8 > 8, i.e., above 2σ). Light grey dots: individual GOODS–*Herschel* galaxies normalized to $L_{\mathrm{IR}}^{\mathrm{tot}} = 10^{11}$ $L_\odot$. The large filled symbols with error bars are the median and associated uncertainty of the MS (*left figure*, blue dots) and SB (*right figure*, red dots) galaxies computed in intervals of wavelengths defined to contain a fixed number of 25 ± 5 galaxies. The uncertainty on the median values is derived from the 16th and 84th percentiles around the median divided by the square root of the number of galaxies. The model fit to each SED is shown with a solid black line while the opposing SED (MS or SB) is shown with a dotted black line for comparison.

Main Sequence of Star Forming Galaxies

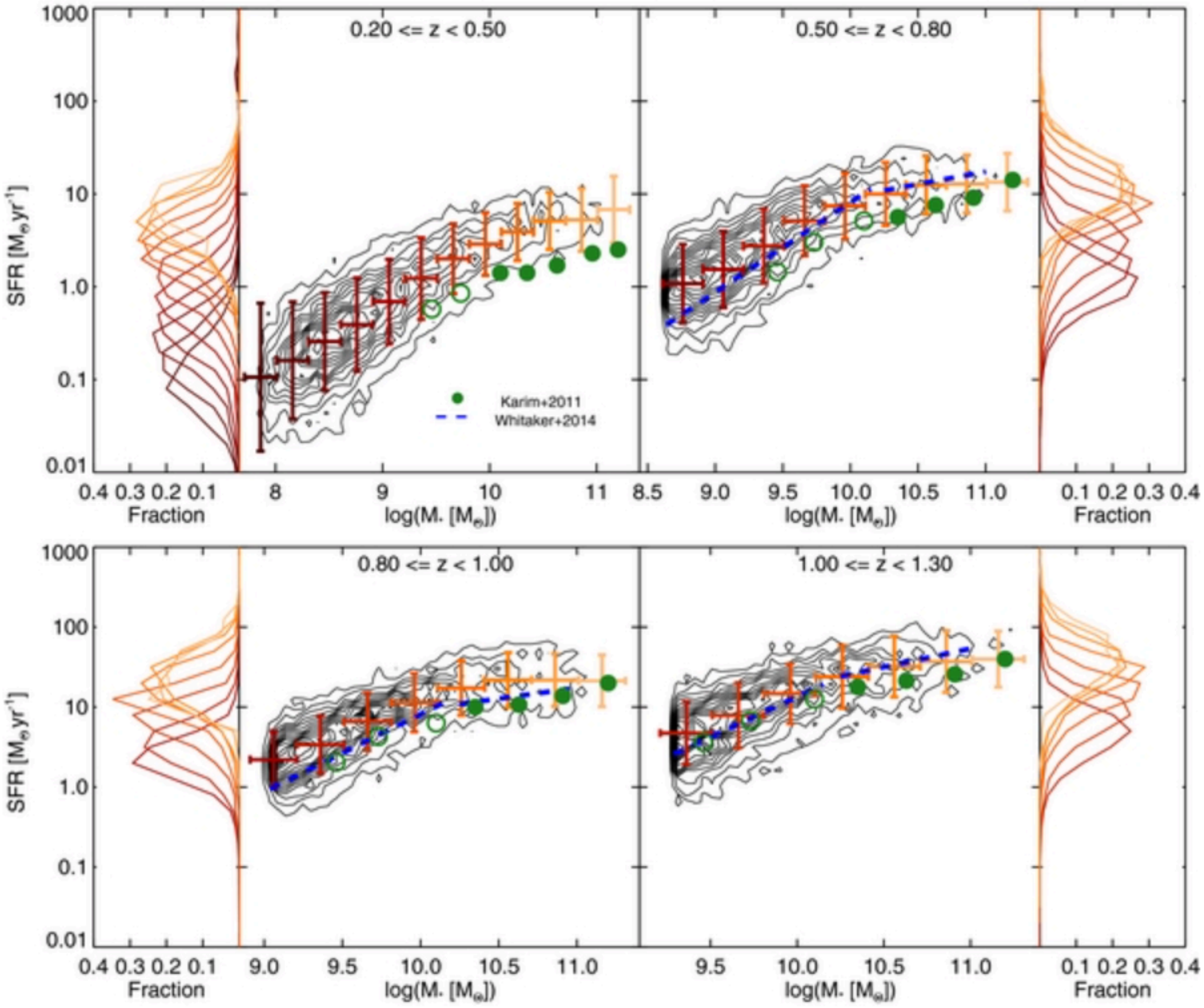

Figure 4. Contour density plot of star-forming galaxies in the COSMOS field.

At all redshifts, the relationship between median SFR and M_* follows a power law at low stellar masses, and flattens to nearly constant SFR at high stellar masses.

Galaxies more massive than $M_* \gtrsim 10^{10} M_\odot$ have a much lower average specific star formation rate (sSFR) than would be expected by simply extrapolating the traditional linear fit to the main sequence found for less massive galaxies.

Main Sequence of Star Forming Galaxies

Fig. 2.10 Evolution of the average SFR of star-forming galaxies with mass and redshift. Our results from stacking are shown as *colored filled circles*, the *colors* corresponding to the different redshifts as indicated in the legend. We complement these measurements by stacking sliding bins of mass (see text) for visualization purposes only to better grasp the mass dependence of the SFR. In the background, we show as *light gray curves* our best-fit relation for the Main Sequence (Eq. 2.9) (color figure online)

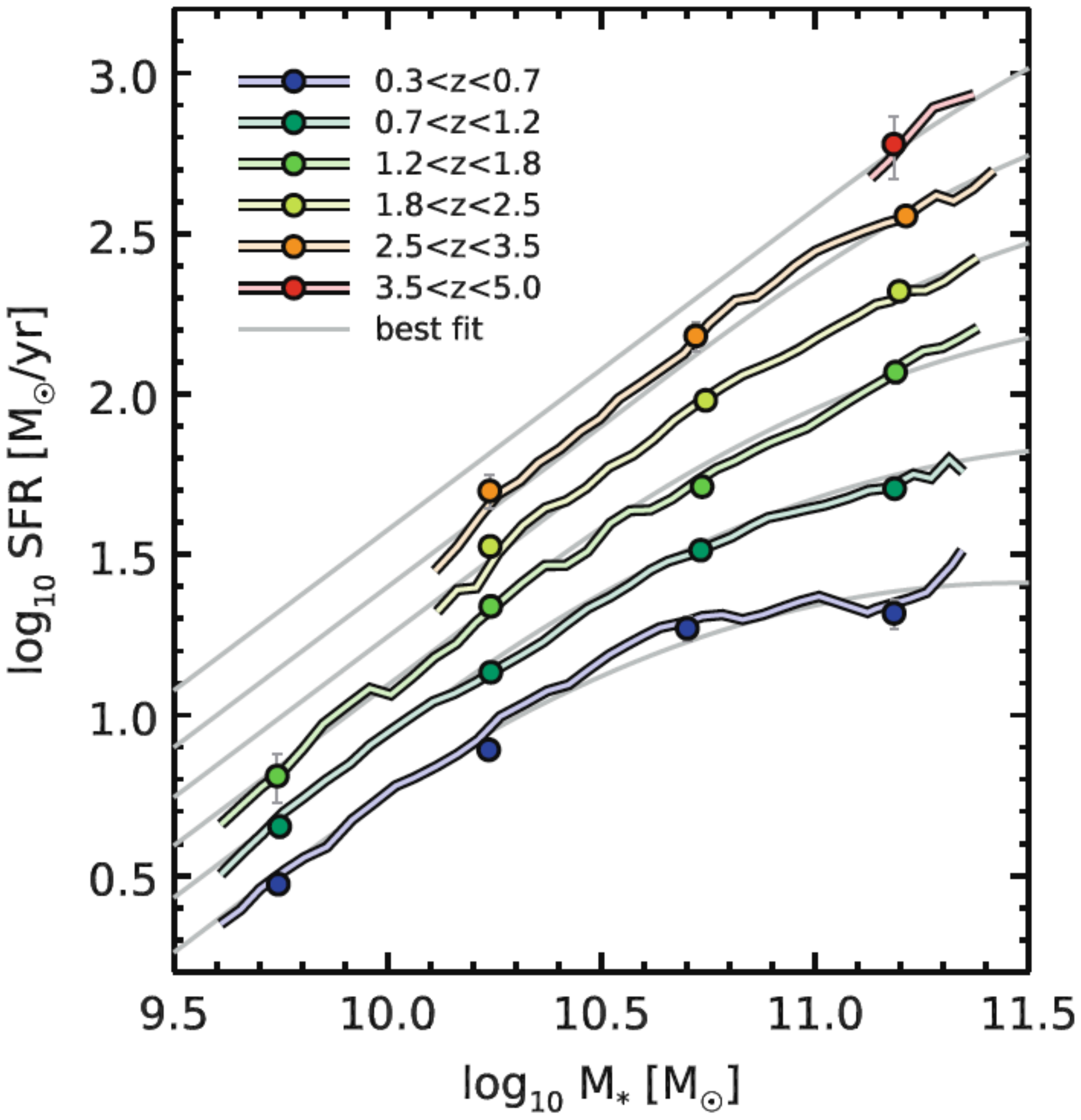

History of cosmic star formation

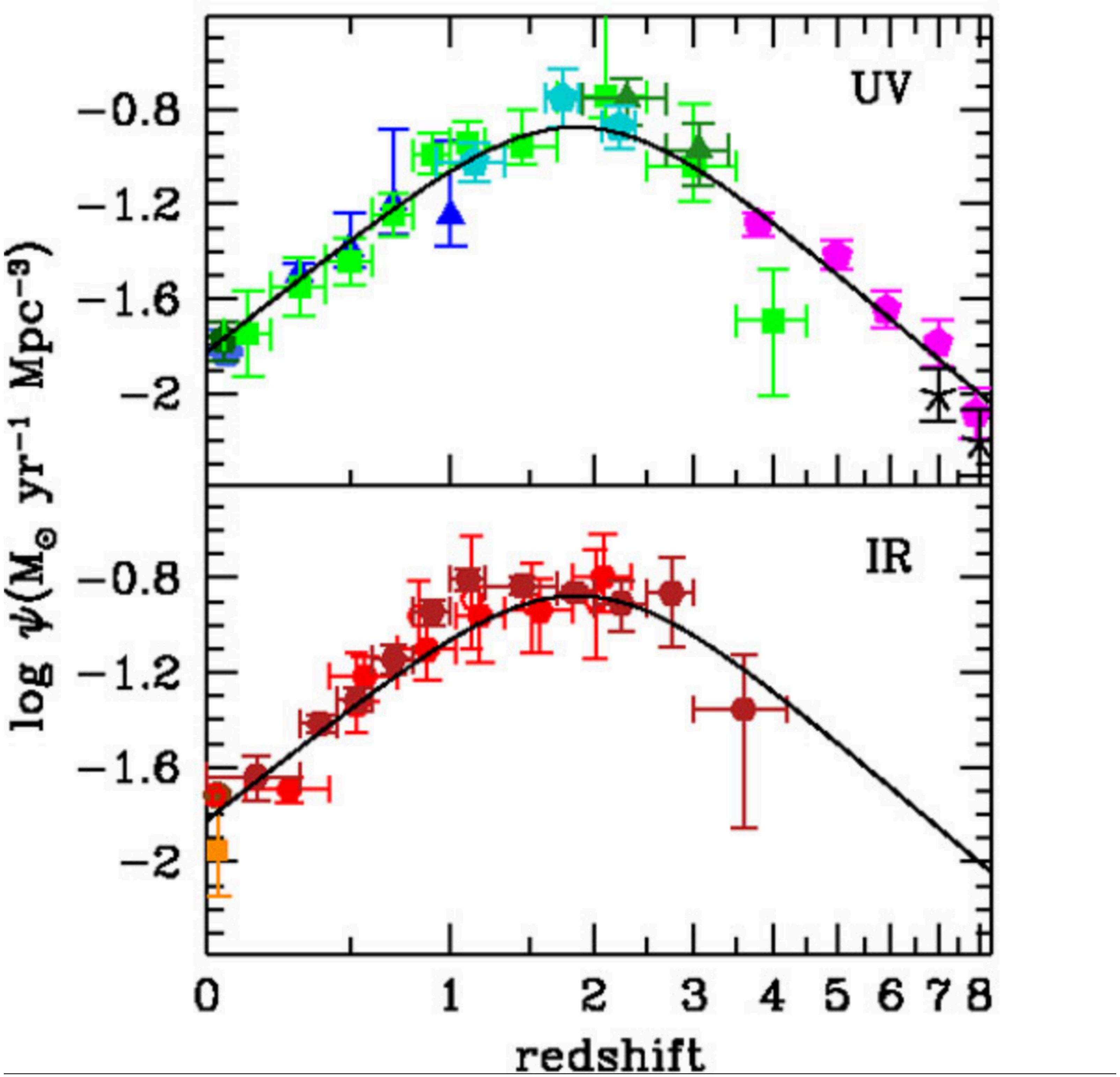

History of cosmic star formation

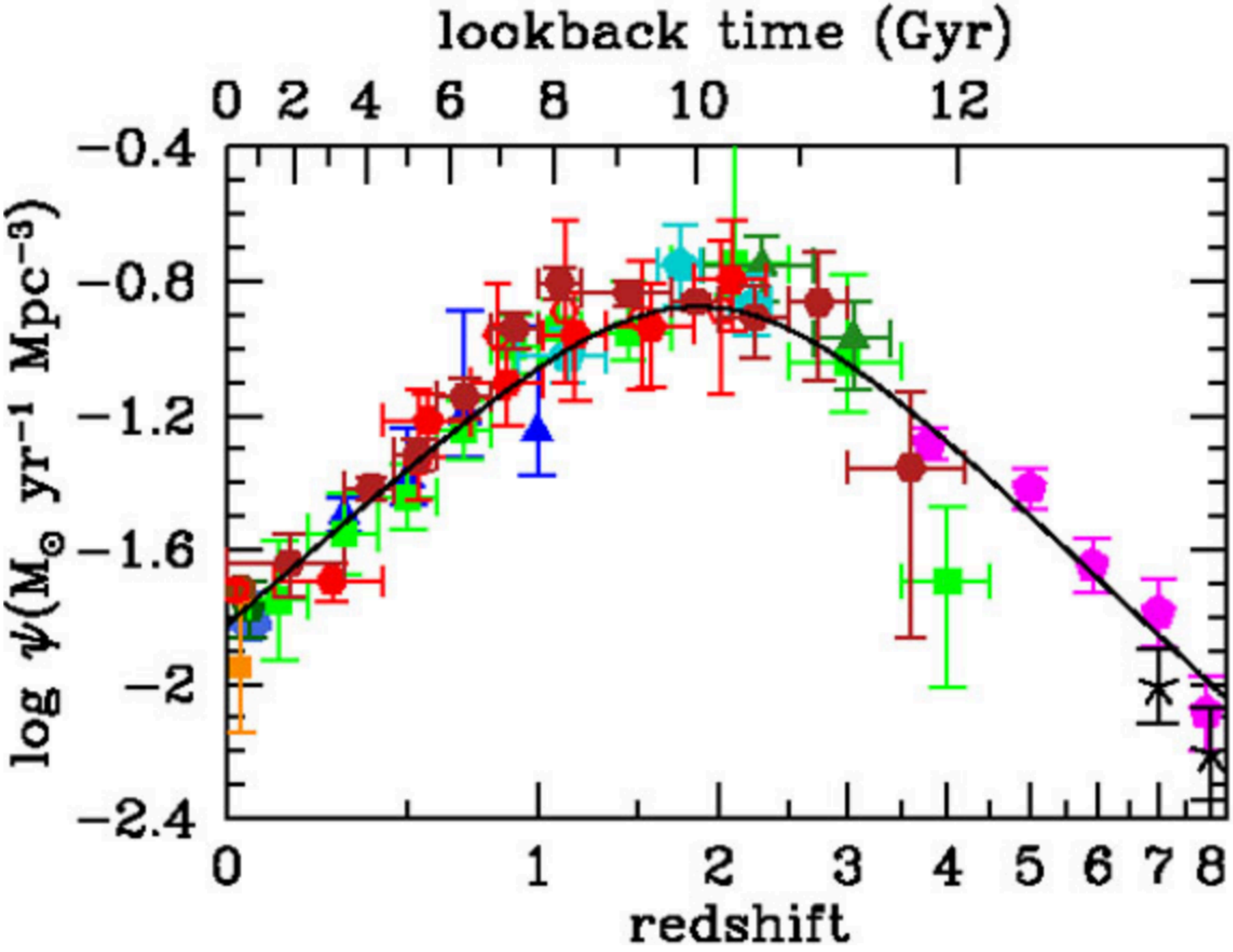

FUV+IR

History of cosmic star formation

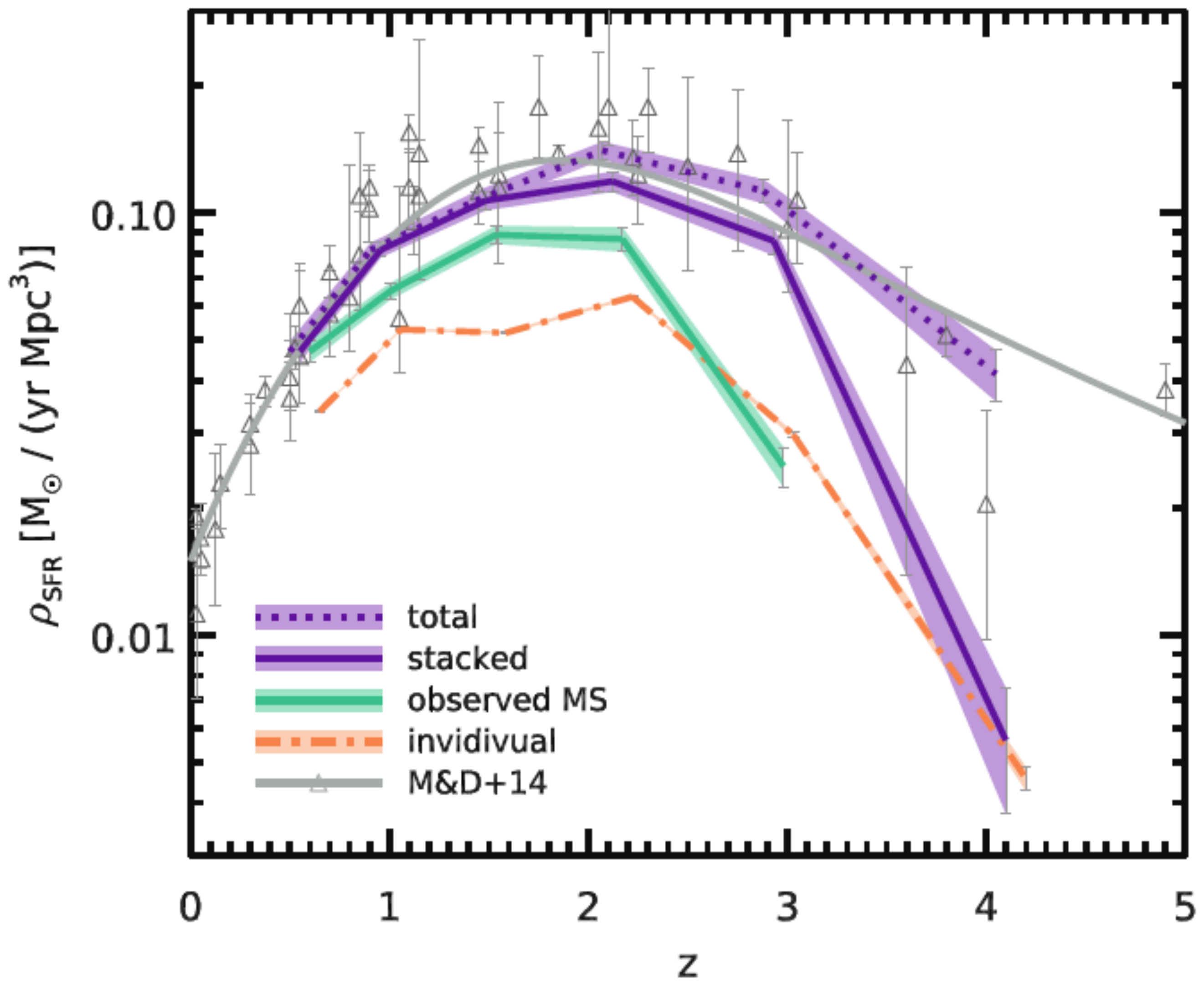

Fig. 2.13 Evolution of the cosmic star formation rate density ρ_{SFR} with redshift. The *orange dash-dotted line* traces the SFR density inferred from individual *Spitzer* MIPS (for $z < 1.5$) and *Herschel* detections alone. The *solid purple line* represents the contribution of stacked sources with significant signal ($>5\sigma$), and the *dotted line* is the extrapolation of the stacked SFR down to $M_* = 3 \times 10^9$ M$_\odot$ assuming constant sSFR and using the mass functions of Fig. 2.3. The *green line* shows the fraction of ρ_{SFR} in regimes where we have probed the existence of the Main Sequence. The *lines* are slightly offset in redshift for clarity. *Light shaded regions* in the background show the corresponding 1σ statistical errors. We compare these to the literature compilation of Madau and Dickinson (2014), shown as *open triangles*, with their best-fit plotted as a *solid gray line* (color figure online)

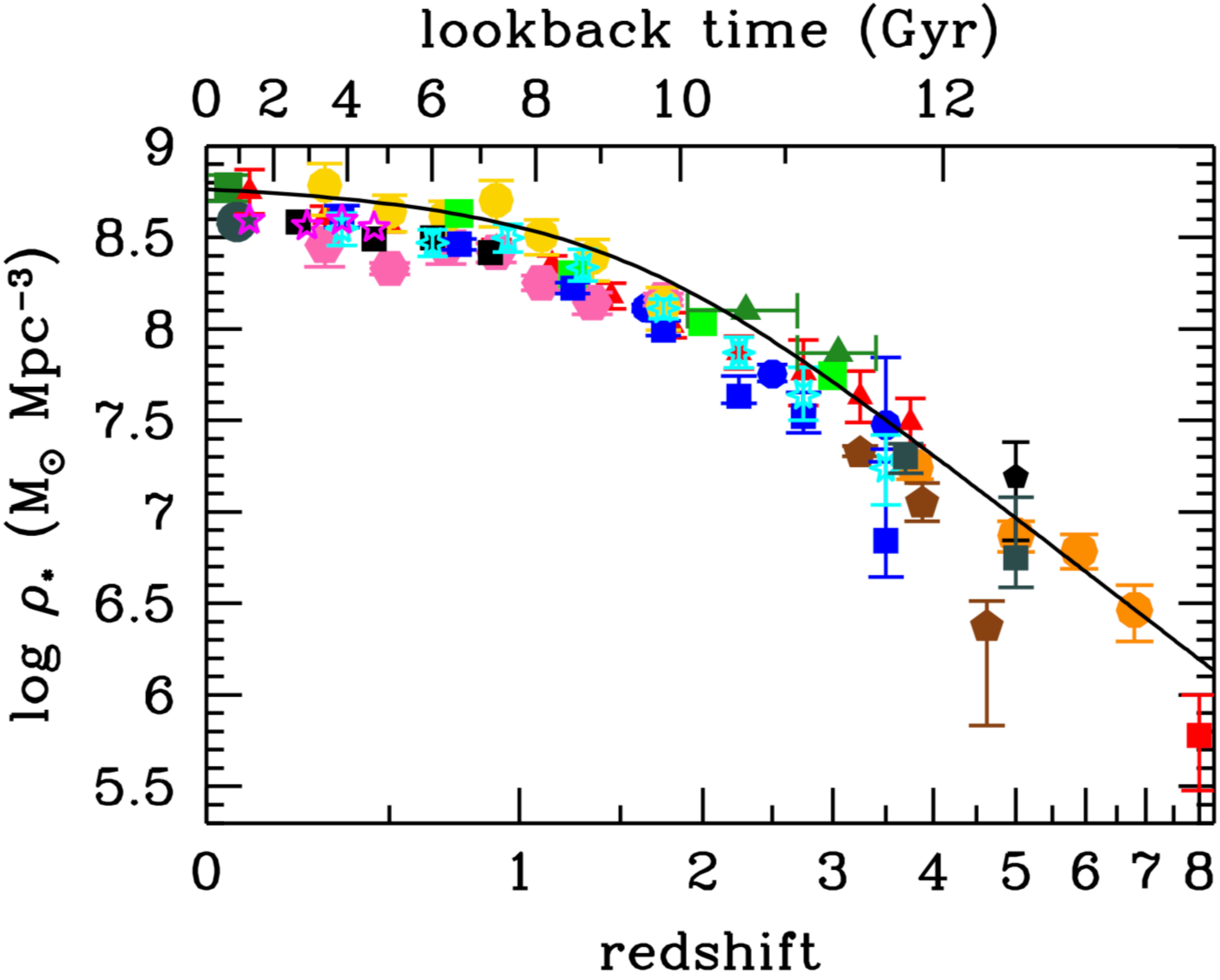

Figure 11: The evolution of the stellar mass density. The data points with symbols are given in Table 2. The solid line shows the global stellar mass density obtained by integrating the best-fit instantaneous star-formation rate density $\psi(z)$ (Equations 2 and 15) with a return fraction $R = 0.27$.